Evaluation of turbulence closure models under spilling and plunging breakers in the surf zone.

S.A. Brown, D.M. Greaves, V. Magar, D.C. Conley

Please cite this article as:

Brown, S.A., Greaves, D.M., Magar, V. and Conley, D.C. (2016). Evaluation of turbulence closure models under spilling and plunging breakers in the surf zone, Coastal Engineering, doi: 10.1016/j.coastaleng.2016.04.002

Evaluation of turbulence closure models under spilling and plunging breakers in the surf zone.

S. A. Brown[a,*], D. M. Greaves[a], V. Magar[b], D. C. Conley[a]

[a] *School of Marine Science and Engineering, Plymouth University, Plymouth, United Kingdom*
[b] *Department of Physical Oceanography, CICESE, Ensenada, Mexico*

Abstract

Turbulence closure models are evaluated for application to spilling and plunging breakers in the surf zone using open source computational fluid dynamics software. A new library of turbulence models for application to multiphase flows has been developed and is assessed for numerical efficiency and accuracy by comparing against existing laboratory data for surface elevation, velocity and turbulent kinetic energy profiles. Out of the models considered, it was found that, overall, the best model is the nonlinear $k - \epsilon$ model. The model is also shown to exhibit different turbulent characteristics between the different breaker types, consistent with experimental data.

Keywords:
spilling breakers, plunging breakers, turbulence models, computational fluid dynamics, OpenFOAM, surf zone

1. Introduction

In environments where a large quantity of fine sand is found, suspended sediment concentrations, and therefore transport, can become very significant. These suspended loads can have a great impact on physical and biological processes, for instance, coastal erosion and light penetration through the water column. Therefore, it is essential to be able to predict suspended sediment concentrations and sediment transport rates with good accuracy. As a consequence, substantial research effort has been put into understanding the processes behind suspended sediment dynamics in both the surf and swash zones (Puleo et al., 2003; van Rijn, 2007).

A significant consideration when predicting suspended sediment concentrations in the surf and swash zones, is the effect of breaking waves and the associated turbulence (Falchetti et al., 2010). In the surf zone, breaking waves

*Corresponding author
Email address: scott.brown@plymouth.ac.uk (S. A. Brown)

generate turbulence to levels capable of suspending and transporting large quantities of sediment. Such breaker-induced turbulence is influenced mainly by the Iribarren number, ξ_0, (Battjes, 1974; Iribarren and Nogales, 1949), linking the breaker's steepness and the beach slope. The value of the Iribarren number indicates the type of breaker, defined as spilling ($\xi_0 < 0.5$), plunging ($0.5 < \xi_0 < 3.3$) or collapsing ($3.3 < \xi_0$). A number of experimental investigations have been conducted on the dynamics of turbulence generated on a sloping beach by both spilling (Ting and Kirby, 1994, 1996; Govender et al., 2002; Huang et al., 2009) and plunging breakers (Ting and Kirby, 1994, 1995; Kimmoun and Branger, 2007). Many numerical models have also been developed to consider this problem. A number of these models have made use of a two equation turbulence model to represent turbulence generation and dissipation in the surf zone, with varying results, although they generally overestimate the levels of turbulent kinetic energy (TKE) generated by the breakers. A variety of two equation turbulence closure models has been applied in these numerical models; the $k-\epsilon$ (Bradford, 2000; Xie, 2013; Ma et al., 2014), $k-\omega$ (Christensen et al., 2000; Jacobsen et al., 2012), RNG $k-\epsilon$ (Bradford, 2000) and a nonlinear $k-\epsilon$ model (Lin and Liu, 1998a,b). However, to the authors best knowledge a thorough comparison of two equation turbulence models for spilling and plunging breakers in the surf zone has not been performed using the same code, although Bradford (2000) did compare the standard and RNG $k-\epsilon$ models.

In this work, five turbulence closure models are thoroughly evaluated for accuracy in predictions of surface elevation, horizontal velocity and TKE, in relation to experimental data for both spilling and plunging breakers. The open source computational fluid dynamics (CFD) code, "OpenFOAM" (OpenFOAM, 2014) based on the Reynolds Averaged Navier-Stokes (RANS) equations is utilised along with waves2Foam, a wave generation toolbox developed by Jacobsen et al. (2012). Following Jacobsen (2011), a new library of turbulence models has been created within the OpenFOAM environment, which account for density variations around the free surface (Brown et al., 2014). The surface elevation, velocity and TKE data used for comparison has been gathered by Ting and Kirby (1994), through a thorough set of laboratory experiments into both spilling and plunging breakers on a beach of gradient 1/35. The results were obtained by producing cnoidal waves and phase-averaging (denoted by a tilde, i.e. $\widetilde{\eta}$) the waves over a period of twenty minutes. The fluid velocities were obtained using a fibre-optic laser-Doppler anemometer and the TKE values were then calculated by the formula

$$k = \frac{2}{3}(\widetilde{u'^2} + \widetilde{w'^2}), \tag{1}$$

where u' and w' are the fluctuations from the mean velocity. Since only one component of the velocity could be measured at a time, the horizontal and vertical velocity time series, and subsequently the TKE, was obtained from separate twenty minute runs.

The paper is organised as follows. First, an overview of the turbulence models is given. Then, the numerical setup is presented, followed by a comparison

of the turbulence models against laboratory data. Finally, the conclusions are drawn.

2. Turbulence Models

This work focuses on four popular two equation turbulence closure models ($k-\omega$, $k-\omega$ SST, RNG $k-\epsilon$, nonlinear (NL) $k-\epsilon$) and a Reynolds stress model (RSM), which solves for all components of the Reynolds Stress (Launder et al., 1975). All of the two equation models use an eddy viscosity to calculate the Reynolds stress, obtained by solving equations for the turbulent kinetic energy (TKE), k, and either the turbulence dissipation rate, ϵ, ($k-\epsilon$ models) or a characteristic frequency, ω, associated with the turbulence ($k-\omega$ models). This section describes the different models used and the advantages and disadvantages of each.

$k-\epsilon$ models are a commonly used method for turbulence closure. Hence, the weaknesses of the standard $k-\epsilon$ model are generally well known. One of these weaknesses is that the transport equation for ϵ becomes singular near the wall, so, in order to model the viscous sublayer accurately, it is necessary to introduce damping at the wall. Furthermore, fully developed, isotropic turbulence is assumed, so the model generally under-performs under transitional turbulence or adverse pressure gradients (Versteeg and Malalasekera, 1995; Wilcox, 2006). The renormalised group (RNG) $k-\epsilon$ aims to address some of the weaknesses of the standard $k-\epsilon$ model. Originally developed using an additional expansion parameter by Yakhot et al. (1992), the RNG $k-\epsilon$ has been shown to perform better than the standard $k-\epsilon$ model in transitional flows (Versteeg and Malalasekera, 1995). However, the additional expansion parameter causes the model to become overly sensitive to the magnitude of the strain rate. Furthermore, the model is also based upon the assumption of isotropy, which is not valid for all flows.

Another model being evaluated is the $k-\omega$ model (Wilcox, 2006). It offers improved near wall treatment, removing the necessity for wall damping. It has also been shown to give more accurate predictions, than the standard $k-\epsilon$ model, in cases of adverse pressure gradients (Wilcox, 2006). However, it can be overly sensitive to the inlet free stream boundary conditions and still relies on the isotropic turbulence assumption. A variation on this model is the $k-\omega$ shear stress transport (SST) model, developed by Menter (1994) and is a blend of both the $k-\omega$ and $k-\epsilon$ model. It aims to address the sensitivity to the free stream value of ω, whilst keeping the improved near wall treatment. To achieve this, a blending function is utilised, which applies the $k-\omega$ model for near wall treatment and the $k-\epsilon$ in the free stream. However, not all of the problems with $k-\omega$ and $k-\epsilon$ models are fixed by this method, since it also assumes that turbulence is isotropic.

In this study, the validity of the isotropic assumption is considered in two ways. The first is to use the nonlinear $k-\epsilon$ model developed by Shih et al. (1996), which accounts for anisotropic effects by introducing a nonlinear Reynolds stress term into the standard $k-\epsilon$ model. Shih et al. (1996) showed that the nonlinear

$k-\epsilon$ model performs better than the standard $k-\epsilon$ model for flows under strong adverse pressure gradients, as well as for separated and swirling flows. The second model is a Reynolds stress model (RSM) developed by Launder et al. (1975). This model resolves all directions of the Reynolds stress directly, along with an equation for ϵ for closure, eliminating the need for an eddy viscosity and hence the assumptions on the isotropy of the turbulence. This model is expected to produce the most accurate results since it captures the physics more realistically, but at the cost of computational efficiency since seven equations are solved. However, it uses the same ϵ equation as the isotropic turbulence models, indicating that if this is not modelled correctly then it will perform no better than the other models considered in this study.

3. Numerical Model

The turbulence models discussed in Section 2 are tested for 2D spilling and plunging breakers propagating perpendicular to the shore. The free surface is tracked using a two-phase volume of fluid (VOF) technique, solved together with the incompressible RANS equations for the fluid flow field. The coordinate system (x, y, z) is taken such that x corresponds to the cross-shore direction, with positive x in the direction of wave propagation. The waves are generated on the left at the Inlet boundary and propagate towards a beach located on the right of the domain (see Figure 1). y and z are the long-shore and vertical coordinates, respectively. Waves are generated at the Inlet by setting a time-dependent boundary condition for the velocity and the free surface, both based on analytical solutions of the wave equations. A relaxation zone at the Inlet permits absorption of wave reflections at the boundary. A Courant number of 0.2 for the spilling and 0.1 for the plunging breaker cases was found to be necessary for numerical stability. The mesh has been designed using a mesh convergence study to ensure that a mesh independent solution is obtained with minimum computational expense. Two approaches were considered; both refining the whole computational domain and refining the region around the free surface only. Time series' of velocity, surface elevation and TKE were then compared to determine when a mesh independent solution had been achieved. To further minimise numerical diffusion, higher order numerical schemes (e.g. linear rather than upwind) were used where numerical stability allowed.

3.1. Computational Domain & Boundary Conditions

The computational domain is setup to be consistent with the laboratory experiments of Ting and Kirby (1994) and is illustrated in Figure 1. There is a sloping beach of gradient 1/35, the water depth, h, is 0.4 m and the origin is located at the still water line, 0.7 m shoreward of the start of the slope, where $h = 0.38$ m (see Figure 1). Approximately 320000 cells are used to discretise the domain in the spilling breakers case, whereas 360000 cells are used for the plunging breakers. The domain is only one cell thick in the y direction, and in the x and z directions, the cells have an aspect ratio of 1 where possible,

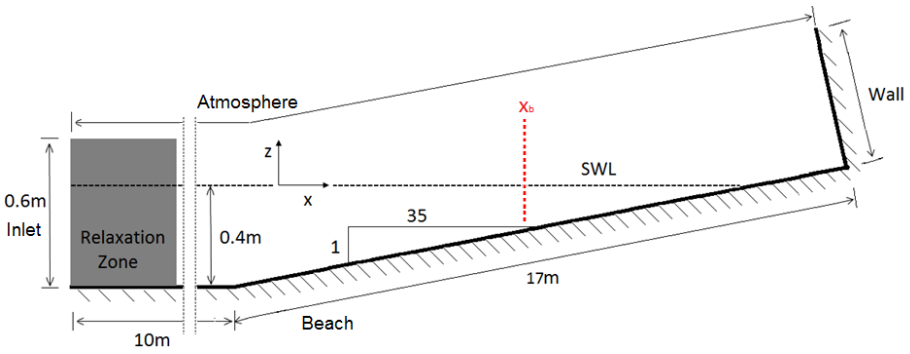

Figure 1: Diagram of the computational domain (not to scale) and the boundary names used.

i.e. $\Delta x = \Delta z$, for both cases. This was shown to improve the breaking point and height of the wave by Jacobsen et al. (2012), who suggested that this was due to larger VOF flux in cells of aspect ratio greater than one. The cell size in the internal domain is set to 0.01 m and, based on a balance of accuracy and CPU time, determined through the previously mentioned mesh refinement study, further refinement has been applied in the x and z directions around the free surface. Therefore, the discretisation is 0.005 m in this region. At the Beach boundary six layers of thinner cells (in the z direction) have been used, with each layer away from the boundary being twice the size of the last.

Regular waves are generated by stream function wave theory (Rienecker and Fenton, 1981) at the Inlet boundary. The spilling breakers are created by incoming, regular waves of period $T = 2\,\mathrm{s}$ and height $H = 0.125\,\mathrm{m}$, whereas the plunging breakers are generated using $T = 5\,\mathrm{s}$ and height $H = 0.127\,\mathrm{m}$. A relaxation zone is applied at the Inlet boundary for both cases; for the spilling breakers the relaxation zone is approximately one wavelength L long, whereas in the plunging case it is $L/2$. This has been shown to allow simulation, and therefore averaging, over a large number of waves (Jacobsen et al., 2012). The model is run for fifty wavelengths, with the final twenty waves averaged and used for the results in this study. Data is collected relative to the breaking point of the wave at the probe locations considered by Ting and Kirby (1994).

The Beach and Wall boundaries are considered as solid walls and therefore no-slip conditions have been applied along with zero gradient conditions for pressure and VOF. The top boundary also uses a Neumann boundary condition for the VOF but the boundary condition for the velocity varies according to the near boundary flux; using a zero gradient condition for outflow and the internal cell value of the normal component to the patch face for the inflow. The top boundary condition for pressure is defined as the total pressure

$$p = p_0 + \frac{1}{2}|\mathbf{u}|^2 \tag{2}$$

where p_0 is the user defined reference value, and $\mathbf{u}$ is the velocity. For this case p_0 is set to zero since the solver uses the difference between total pressure and

hydrostatic pressure. The initial conditions are set to the solution obtained after running the model without a turbulence model turned on for fifty wavelengths.

Wall functions are applied at the Beach boundary. The wall functions switch between low Reynolds number (LRN) and high Reynolds number (HRN) flows, depending on whether the near wall cell centre lies in the log or laminar sublayer. This is evaluated through the dimensionless wall distance

$$z^+ = \frac{\Delta z_w u_*}{\nu} = \frac{\Delta z_w \sqrt[4]{C_\mu}\sqrt{k}}{\nu}, \tag{3}$$

where Δz_w is the distance from the near wall cell centre to the wall. Comparing z^+ to the threshold value at the edge of the laminar sublayer, z^+_{lam}, gives an indication as to the region in which the near wall centre lies. The value of z^+_{lam} is obtained by solving

$$z^+_{lam} = \frac{\log(z^+_{lam}E)}{\kappa} \tag{4}$$

where E is an integration constant associated with the surface roughness and κ is the von Kármán constant. If $z^+ > z^+_{lam}$, the cell centre is assumed to be in the log layer and a HRN wall function is used. Conversely, if $z_+ \leq z^+_{lam}$ then the cell centre is assumed to be below the log layer and therefore a LRN wall function is used. Neumann boundary conditions are applied for each of the turbulent variables at the Wall boundary. At all the other boundaries the turbulent boundary conditions must be chosen carefully since, although TKE should not exist at the walls, Lin and Liu (1998a) note that the transport equations become singular if $k = 0$, making it necessary to 'seed' a small quantity of TKE. Following Lin and Liu (1998a), the TKE at the Inlet is calculated as

$$k = \frac{1}{2}(c_p I)^2 \tag{5}$$

where I and $c_p = L/T$ are the turbulence intensity and phase speed of the wave, respectively. The ϵ or ω value is then adjusted so that the eddy viscosity is a fraction, λ, of the kinematic viscosity, i.e. $\nu_t = \lambda\nu$. Following Lin and Liu (1998a), I and λ are chosen as 0.0025 and 0.1, respectively, in this study. The initial conditions are set to the value specified at the Inlet.

3.2. Implementation of Turbulence Models

In this section, the transport equations for each of the turbulence models under consideration are discussed with particular emphasis on how they are implemented in OpenFOAM (v. 2.1.1). The general form of the equations is such that

$$\begin{aligned} \textit{rate of change} + \textit{transport by convection} = \textit{production} - \textit{dissipation} \\ + \textit{transport by diffusion.} \end{aligned}$$

Each model has two transport equations, one for TKE (other than the Reynolds stress model which solves for the Reynolds stress, $\boldsymbol{\tau}$) and another for either ϵ or

ω. The values obtained from solving these equations are then used to compute the eddy viscosity. For the models which do not solve an equation for $\boldsymbol{\tau}$, the eddy viscosity is used to model the Reynolds stress through the relationship

$$\boldsymbol{\tau} = \frac{2}{3}k\mathbf{I} - 2\nu_t\mathbf{S}, \tag{6}$$

where $\mathbf{S}$ is the mean rate of strain of the flow defined as

$$\mathbf{S} = \frac{1}{2}(\nabla\mathbf{u} + \nabla\mathbf{u}^T). \tag{7}$$

It is worth noting that all of the incompressible solvers implemented in OpenFOAM, including those for multiphase flows, do not include density explicitly but instead model the kinematic eddy viscosity, ν_t rather than the dynamic form, μ_t. However, Brown et al. (2014) have shown that for simulations of breaking waves using the VOF method, more accurate results are obtained by including the density explicitly in the turbulence transport equations and therefore in this work a new library of turbulence models, within the OpenFOAM environment, has been developed to reflect this.

3.2.1. The $k-\omega$ model

The $k-\omega$ model originally developed by Wilcox (1988), solves the following transport equations for k and ω,

$$\frac{\partial\rho k}{\partial t} + \nabla\cdot(\rho\mathbf{u}k) = P_k - \rho C_\mu\omega k + \nabla\cdot[\rho(\nu+\sigma_k\nu_t)\nabla k], \tag{8}$$

$$\frac{\partial\rho\omega}{\partial t} + \nabla\cdot(\rho\mathbf{u}\omega) = \frac{\gamma\omega}{k}P_k - \rho\beta\omega^2 + \nabla\cdot[\rho(\nu+\sigma_\omega\nu_t)\nabla\omega], \tag{9}$$

with $\sigma_k = \sigma_\omega = 0.5$, $C_\mu = 0.09$, $\beta = 0.072$ and $\gamma = 0.52$. The production term is defined as $P_k = \rho\nu_t|S|^2$, defining S, in terms of $\mathbf{S}$, as $S = \sqrt{2\mathbf{S}\mathbf{:}\mathbf{S}}$, where $\mathbf{:}$ is the double inner product. The values of k and ω are obtained by solving equations (8) and (9), and are then used to compute the eddy viscosity, $\nu_t = k/\omega$.

3.2.2. The $k-\omega$ SST model

Menter (1994) originally developed the $k-\omega$ SST model, which solves the equations

$$\frac{\partial\rho k}{\partial t} + \nabla\cdot(\rho\mathbf{u}k) = \min\left(P_k, \rho c_1 C_\mu k\omega\right) - \rho C_\mu\omega k + \nabla\cdot[\rho(\nu+\sigma_k\nu_t)\nabla k], \tag{10}$$

$$\frac{\partial\rho\omega}{\partial t} + \nabla\cdot(\rho\mathbf{u}\omega) = \frac{\gamma P_k}{\nu_t} - \rho\beta\omega^2 + \nabla\cdot[\rho(\nu+\sigma_\omega\nu_t)\nabla\omega] + 2\rho(1-F_1)\frac{\sigma_{\omega 2}}{\omega}\nabla k\cdot\nabla\omega, \tag{11}$$

where P_k is the same as in the $k-\omega$ model. The coefficients σ_k, σ_ω, β and γ are a blend of an inner constant (subscript 1) and an outer constant (subscript 2), blended according to

$$\phi = F_1\phi_1 + (1-F_1)\phi_2. \tag{12}$$

The function $F_1 = \tanh(\Gamma_1^4)$ used in the blending function, depends upon the argument Γ_1 described by

$$\Gamma_1 = \min\left(\min\left(\left[\max\left\{\frac{k}{C_\mu\omega\Delta z_w}, \frac{500\nu}{\Delta z_w^2\omega}\right\}\right], \frac{4\sigma_{\omega 2}k}{CD_{k\omega}\Delta z_w^2}\right), 10\right), \tag{13}$$

where

$$CD_{k\omega} = \max\left\{\frac{2\sigma_{\omega 2}}{\omega}\nabla k\cdot\nabla\omega, 10^{-10}\right\}, \tag{14}$$

and Δz_w is the distance from the field point to the nearest wall. The values for the inner and outer constants are given in Table 1. The eddy viscosity is then calculated by

$$\nu_t = \frac{a_1 k}{\max\{a_1\omega, b_1 F_2\sqrt{2}S\}}, \tag{15}$$

where

$$F_2 = \tanh(\Gamma_2^2), \qquad \Gamma_2 = \min\left(\max\left\{\frac{2\sqrt{k}}{\omega\Delta z_w}, \frac{500\nu}{\Delta z_w^2\omega}\right\}, 100\right). \tag{16}$$

σ_{k1}	σ_{k2}	$\sigma_{\omega 1}$	$\sigma_{\omega 2}$	β_1	β_2	γ_1	γ_2
0.85034	1.0	0.5	0.85616	0.075	0.0828	0.5532	0.4403

Table 1: Default values for the inner and outer constants in the $k-\omega$ SST model.

3.2.3. The RNG $k-\epsilon$ model

The Renormalised group (RNG) $k-\epsilon$ model solves two equations for k and ϵ defined as

$$\frac{\partial\rho k}{\partial t} + \nabla\cdot(\rho\mathbf{u}k) = P_k - \rho\epsilon + \nabla\cdot[\rho(\nu+\sigma_k\nu_t)\nabla k], \tag{17}$$

$$\frac{\partial\rho\epsilon}{\partial t} + \nabla\cdot(\rho\mathbf{u}\epsilon) = \frac{C_{1\epsilon}^* P_k\epsilon}{k} - \frac{\rho C_{2\epsilon}\epsilon^2}{k} + \nabla\cdot[\rho(\nu+\sigma_\epsilon\nu_t)\nabla\epsilon]. \tag{18}$$

The coefficient $C_{1\epsilon}^*$ differs between the standard $k-\epsilon$ and RNG $k-\epsilon$ models (Speziale and Thangam, 1992). In the former it is just $C_{1\epsilon}$ and in the latter is derived as

$$C_{1\epsilon}^* = C_{1\epsilon} - \frac{\eta(1-\eta/\eta_0)}{1+\beta\eta^3}. \tag{19}$$

In equation (19), η is the additional expansion parameter used in the derivation by Yakhot et al. (1992), defined as the time scale ratio of the turbulent to the mean strain rate, $\eta = Sk/\epsilon$. The eddy viscosity is computed by

$$\nu_t = C_\mu\frac{k^2}{\epsilon}. \tag{20}$$

All of the model coefficients, except β which is obtained through experiments, are obtained through the derivation of the RNG $k-\epsilon$ model and are set to $C_\mu = 0.0845$, $\sigma_k = \sigma_\epsilon = 1.39$, $C_{1\epsilon} = 1.42$, $C_{2\epsilon} = 1.68$, $\eta_0 = 4.38$ and $\beta = 0.012$.

3.2.4. Nonlinear $k-\epsilon$ model

Nonlinear (NL) $k-\epsilon$ models are an alternative to Reynolds stress closure models. In this work, a model developed by Shih et al. (1996) is used, which relates the mean strain rate of the flow to the Reynolds stress tensor through the algebraic nonlinear Reynolds stress model. The model adjusts the Reynolds stress, $\boldsymbol{\tau}$, by adding a nonlinear stress term $\boldsymbol{\tau_{NL}}$, defined as

$$\boldsymbol{\tau_{NL}} = \frac{1}{2}(\boldsymbol{\chi} + \boldsymbol{\chi}^T), \tag{21}$$

$$\boldsymbol{\chi} = \frac{k^3}{(A_2+\eta^3)\epsilon^2}\left(C_{\tau 1}[\nabla\mathbf{u}\cdot\nabla\mathbf{u}+(\nabla\mathbf{u}\cdot\nabla\mathbf{u})^T]+C_{\tau 2}[\nabla\mathbf{u}\cdot(\nabla\mathbf{u})^T]+C_{\tau 3}[(\nabla\mathbf{u})^T\cdot\nabla\mathbf{u}]\right), \tag{22}$$

where $C_{\tau 1}$, $C_{\tau 2}$, $C_{\tau 3}$ and A_2 are constants. The parameter η is defined the same as in the RNG $k-\epsilon$ model, with k and ϵ being calculated using equations (17) and (18), with different values for the coefficients ($C^*_{1\epsilon} = 1.44$, $C_{2\epsilon} = 1.92$, $\sigma_\epsilon = 0.77$, $\sigma_k = 1$). The nonlinear stress term is also used in the production term, P_k, which is defined as

$$P_k = \rho(\nu_t \mathbf{S}\!:\!\nabla\mathbf{u} - \boldsymbol{\tau_{NL}}\!:\!\nabla\mathbf{u}). \tag{23}$$

The eddy viscosity is obtained through the same relationship as in the RNG $k-\epsilon$ (equation 20) except that the value of C_μ depends upon the values of ξ and η,

$$C_\mu = \frac{2}{3(A_1+\eta+\alpha_\xi\xi)}, \tag{24}$$

where α_ξ and A_1 are constants and $\xi = \Omega k/\epsilon$ is an additional parameter, where Ω, defined in terms of the mean rate of rotation, $\boldsymbol{\Omega}$, is

$$\Omega = \sqrt{2\boldsymbol{\Omega}\!:\!\boldsymbol{\Omega}}, \qquad \boldsymbol{\Omega} = \frac{1}{2}\left(\nabla\mathbf{u} - (\nabla\mathbf{u})^T\right), \tag{25}$$

Using the eddy viscosity, the Reynolds Stress, $\boldsymbol{\tau}$, is calculated through the relationship

$$\boldsymbol{\tau} = \frac{2}{3}k\mathbf{I} - \nu_t(\nabla\mathbf{u} + \nabla\mathbf{u}^T) + \boldsymbol{\tau_{NL}}. \tag{26}$$

3.2.5. Reynolds Stress Model

Reynolds stress models (RSM) solve equations for ϵ and all six components of the Reynolds Stress ($\boldsymbol{\tau}$). In this work, a RSM based on the work of Launder

et al. (1975) is applied. All the components of $\boldsymbol{\tau}$ are solved in a single transport equation

$$\frac{\partial \rho \boldsymbol{\tau}}{\partial t} + \nabla \cdot (\rho \mathbf{u} \boldsymbol{\tau}) = \rho(1 - C_{2\tau})\mathbf{P} + \frac{\rho}{3} C_{2\tau} \mathrm{tr}(\mathbf{P})\mathbf{I} - \frac{2\rho}{3}(1 - C_{1\tau})\epsilon \mathbf{I} - \rho C_{1\tau} \frac{\epsilon}{k} \boldsymbol{\tau} + \nabla \cdot [\rho(\nu + \nu_t)\nabla \boldsymbol{\tau}], \tag{27}$$

where $C_{1\tau} = 1.8$, $C_{2\tau} = 0.6$, $\mathbf{I}$ is the identity matrix and $\mathrm{tr}(\mathbf{P})$ represents the trace of matrix $\mathbf{P}$, defined as

$$\mathbf{P} = -\left[\boldsymbol{\tau} \cdot \nabla \mathbf{u} + (\boldsymbol{\tau} \cdot \nabla \mathbf{u})^T \right]. \tag{28}$$

The equation for ϵ is same as the nonlinear $k - \epsilon$ (equation 17) with coefficient values of $C^*_{1\epsilon} = 1.44$, $C_{2\epsilon} = 1.92$, $\sigma_\epsilon = 0.77$, $\sigma_k = 1$) except that the production term is defined as $P_k = 0.5|\mathrm{tr}(\mathbf{P})|$.

TKE is defined as $k = 0.5(u'^2_x + u'^2_y + u'^2_z)$, and can therefore be calculated in this model by taking half the trace of the Reynolds stress, i.e. $k = 0.5tr(\boldsymbol{\tau})$. The eddy viscosity can then be calculated through the same relationship as in the RNG $k - \epsilon$ model (equation 20).

4. Evaluation of Turbulence Models

4.1. Spilling Breakers

Tests are first performed for the spilling breakers case. Comparisons between the model predictions and observations by Ting and Kirby (1994), under the same wave conditions, for the maximum, mean and minimum surface elevation (Figure 2), for the time averaged velocity (Figure 5), and for mean turbulent kinetic energy profiles (Figure 6), are presented.

Figure 2 shows the phase averaged surface elevations $\eta_{max} - \overline{\eta}$, $\overline{\eta}$ and $\eta_{min} - \overline{\eta}$ for the spilling breakers case as a function of horizontal distance, x, along the numerical wave flume. Here η_{max} and η_{min} are the maximum and minimum phase averaged surface elevation and $\overline{\eta}$ is the mean surface elevation. Furthermore, the shaded regions around the maximum and minimum profiles in the figure represent one standard deviation. Each subplot compares a different turbulence closure model to the experimental data (dots) gathered by Ting and Kirby (1994), a) No turbulence model, b) $k - \omega$, c) $k - \omega$ SST, d) RNG $k - \epsilon$, e) nonlinear $k - \epsilon$ and f) RSM. The overall root mean square error (RMSE) for each turbulence model, combining the results for maximum, minimum and mean profiles, is indicated on each plot (denoted by E). The overall RMSE clearly indicates that the RNG and nonlinear $k - \epsilon$ models most accurately reproduce the phase averaged surface elevation out the models considered in this study. If each of the three profiles are considered individually, visual observations and RMSE (for each profile rather than the combined value stated in Figure 2) imply that the RSM captures the minimum and mean profiles the

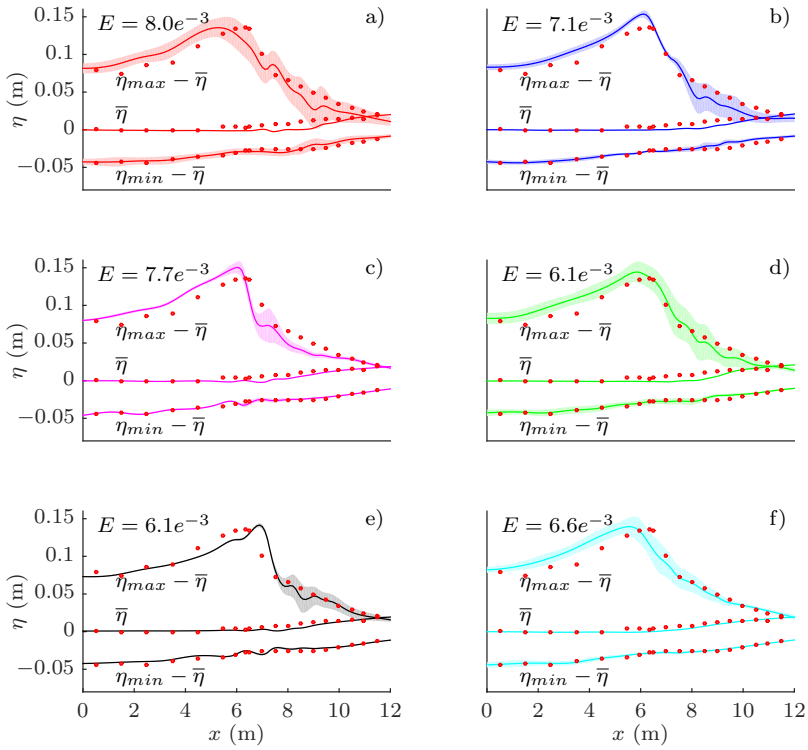

Figure 2: Comparison of surface elevation profiles $\overline{\eta}$, $\eta_{max} - \overline{\eta}$ and $\eta_{min} - \overline{\eta}$ for the spilling breakers. Each subplot represents a different model: a) No Turbulence Model, b) $k - \omega$, c) $k - \omega$ SST, d) RNG $k - \epsilon$, e) NL $k - \epsilon$, f) RSM, with an overall RMSE value, E (representing the maximum, minimum and mean profiles combined), given with respect to the laboratory data gathered by Ting and Kirby (1994), indicated by the dots. One standard deviation either side of the maximum and minimum surface elevations is indicated by the shaded area.

best, although the other models do perform reasonably well with respect to the experimental data. All of the turbulence models capture the wave setup more accurately than when there is no turbulence model used (subplot a), although in general, the wave setup is predicted to occur slightly further along the flume than was shown in the laboratory data. Furthermore, the shaded region shows a much larger variation in maximum and minimum profiles when no turbulence is assumed, suggesting that the waves are more repeatable when a turbulence model is used.

When considering the maximum profiles, there are more obvious differences between the turbulence models. The RNG $k - \epsilon$ model follows the experimental data the closest and has the lowest RMSE for the maximum profile. The $k - \omega$ and $k - \omega$ SST turbulence models all significantly over-estimate the maximum

surface elevation prior to breaking but do predict the breaking point, x_b, at a similar location in the flume as shown in the experiments. The nonlinear $k-\epsilon$ model also over-estimates the breaking height but is the only model to predict the breaking point later than shown in the laboratory. The remaining models all break at a similar height to the experimental data but the breaking point is slightly earlier in the numerical wave flume than expected. Interestingly, the RSM, which solves for all the components of the Reynolds Stress and therefore was expected to be the most accurate model, breaks the earliest of all the turbulence models (but still later than when there is no turbulence model used), 0.8 m earlier than the experimental data. However, it does capture the breaking height well and is the turbulence model which follows the experimental data most accurately in the turbulent bore.

Comparing the shaded profiles before breaking, it is clear that the nonlinear $k-\epsilon$ model and $k-\omega$ SST models have very small variation in both minimum and maximum surface elevation, indicating that every wave is almost identical in terms of wave height. On the other hand, the RSM and RNG $k-\epsilon$ model have reasonable variation prior to breaking, implying that each wave is a slightly different shape. The RNG $k-\epsilon$ model appears to follow the no turbulence model case particularly closely in terms of shape and variation in wave shape at the different regions of the wave flume. It is also interesting to note that the upper envelope of the maximum profile generally captures the profile well after breaking, whereas the mean value under-estimates the shape shown in the physical experiments. As is to be expected, all of the models have a much larger variation after breaking has occurred. This represents that the wave shape is more repeatable, i.e. each wave has a similar shape, before breaking and the waves are less predictable after breaking, which is expected due to the chaotic nature of broken waves.

Figures 3 and 4 emphasise the previously mentioned repeatability of waves prior to breaking and the lack of predictability post-breaking. They show the phase average surface elevation for spilling breakers overlaying the twenty waves used to create the phase average, for the RNG $k-\epsilon$ and nonlinear $k-\epsilon$ models, respectively. The top plot represents the constant depth profile ($x = -1.265$ m) and the bottom post-breaking, in the region with the largest variation ($x = 8.495$ m), as can be seen in Figure 2. Comparing the constant depth profiles, it is clear that every wave has an almost identical wave shape, as is to be expected, when the nonlinear $k-\epsilon$ model is used. On the other hand, for the RNG $k-\epsilon$ model, the twenty waves vary significantly in shape from the phase average profile as was implied in Figure 2. This explains the large variation, relative to the nonlinear $k-\epsilon$ model, in the pre-breaking profile obtained with the RNG $k-\epsilon$. Furthermore, the post-breaking profiles show why there is much larger variation in Figure 2 further down the wave flume. Both turbulence models have large variations in shape, especially in terms of maximum height compared to the phase averaged surface elevation.

Overall, the best models, only taking into account the RMSE, are the nonlinear $k-\epsilon$ and RNG $k-\epsilon$ models. However, the RSM could be considered the best model since it captures the wave setup, as well as the minimum pro-

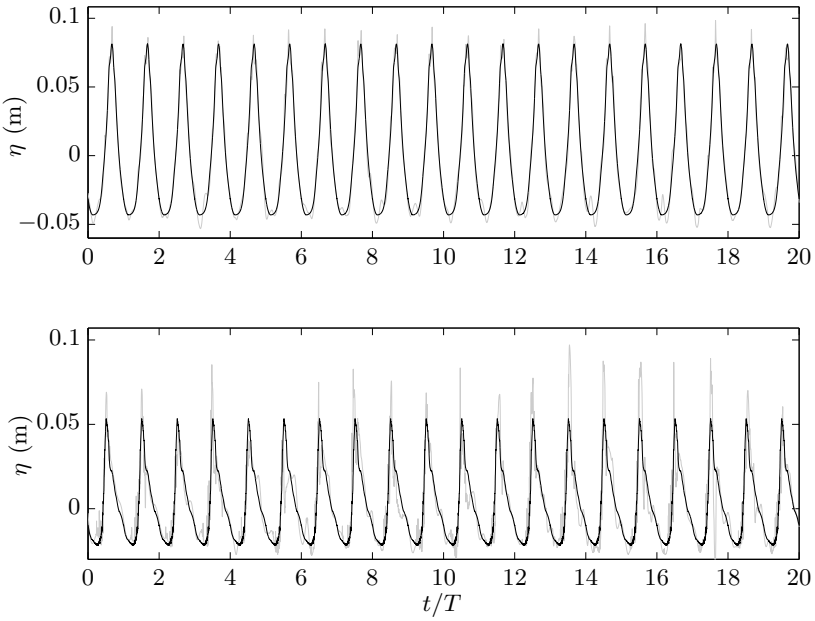

Figure 3: Phase averaged surface elevation (black) overlaying the time series for the twenty waves used to create it (grey) for the spilling breakers case. Both the constant depth region at $x = -1.265\,\mathrm{m}$ (top) and after breaking at $x = 8.495\,\mathrm{m}$ (bottom) for the RNG $k - \epsilon$ model are shown.

file most accurately with respect to the physical experiments. It also captures the maximum profile breaking height and the turbulent bore region well, but the pre-breaking profile is much less accurate than other models. The breaking points of each of the models have been summarised in Table 2, along with the water depths and wave height at breaking.

Figure 5 shows the mean horizontal velocity, $\overline{u}$ ($\mathrm{m\,s^{-1}}$), profiles with dimensionless depth, $(z - \overline{\eta})/h$, for the spilling breakers case. As before the dots represent the experimental data presented by Ting and Kirby (1994). Each row of subplots shows a different sampling location relative to the breaking point, location a is prior to the breaking point (5.945 m in Ting and Kirby (1994)), and locations b-g are post-breaking (6.665, 7.275, 7.885, 8.495, 9.11 and 9.725 m in Ting and Kirby (1994)). Each column of subplots represents a different turbulence closure model, with the no turbulence model case also shown for reference. As a measure of accuracy with respect to the experimental data, the RMSE value (denoted by E) is indicated for each profile at the top of that individual plot. The laboratory data suggests that the mean velocity is negative throughout the majority of the water column with a relatively small region of positive velocity near the free surface. All of the turbulence models capture this change between positive and negative mean velocity, with good agreement in comparison to the

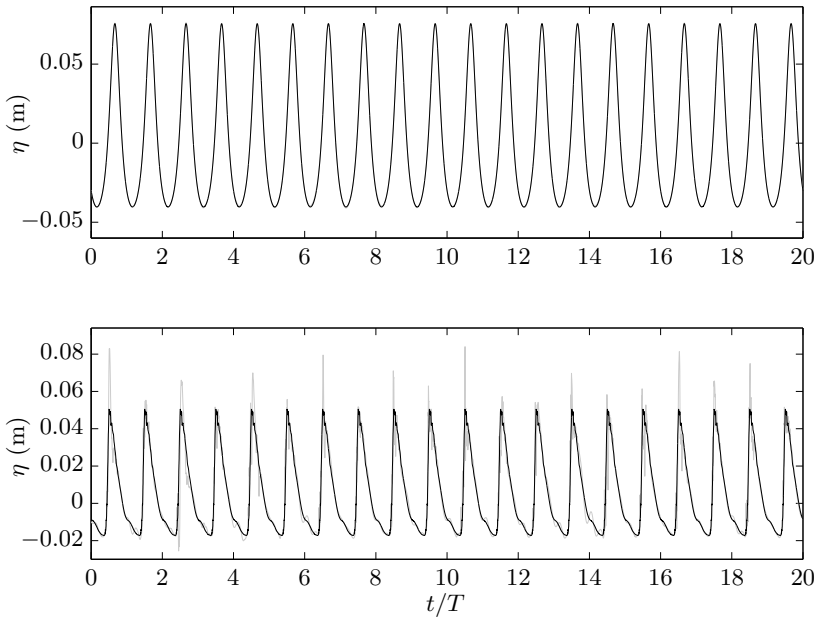

Figure 4: Phase averaged surface elevation (black) overlaying the time series for the twenty waves used to create it (grey) for the spilling breakers case. Both the constant depth region at $x = -1.265\,\mathrm{m}$ (top) and after breaking at $x = 8.495\,\mathrm{m}$ (bottom) for the nonlinear $k - \epsilon$ model are shown.

experimental data.

Another trend in the laboratory data presented by Ting and Kirby (1994) is that the gradient of mean horizontal velocity profile changes sign after breaking has occurred. Around the breaking point (locations a and b), the gradient is negative; the mean velocity is very small near the bottom of the water column, and grows in magnitude closer to the free surface. Further along the wave flume (locations d,e,f and g), a large undertow is present, leading to a positive velocity gradient.

Qualitatively, there is only one turbulence model, the RNG $k - \epsilon$, which captures the negative gradient profile accurately. However, the model does not have the lowest RMSE due to the poor prediction seen in the profile near the top of the water column. Instead the nonlinear $k - \epsilon$ has the lowest RMSE despite not predicting the velocity profile near the bottom of the water column correctly. It is interesting to note that when no turbulence is assumed, the negative gradient is also captured at location a but once breaking occurs there is a significant variation from the experimental data (location b). The remaining models predict similar magnitudes of velocity over the whole water column and therefore perform well closer to the free surface and reduce in accuracy near the bottom.

	No TM	$k-\omega$	$k-\omega$ SST	RNG $k-\epsilon$	NL $k-\epsilon$	RSM	Ting (1994)
x_b	5.3	6.1	6.0	5.9	6.9	5.6	6.4
d_b	0.2286	0.2057	0.2086	0.2114	0.1829	0.2200	0.196
ξ_b	-0.0013	-0.0004	-0.0009	-0.0010	0.0028	-0.0009	0.0033
h_b	0.2273	0.2052	0.2077	0.2105	0.1856	0.2191	0.1993
H_b	0.1679	0.1833	0.1797	0.1744	0.1717	0.1703	0.1621

Table 2: Summary of the spilling breakers information at the breaking point for each turbulence model. x_b is the breaking point, d_b, h_b are the depth from the SWL ($z = 0\,\mathrm{m}$) and MWL ($z = \xi_b\,\mathrm{m}$), respectively, and H_b is the wave height at breaking.

Location c appears to be the transition between the two profile shapes, i.e. where the gradient of the profile changes sign and the mean velocity is almost constant with depth. The turbulence models give very different predictions for this profile, with the RSM and nonlinear $k-\epsilon$ model capturing the shape very well; they appear to keep a similar profile to that predicted at locations a and b where the velocity is almost constant over the depth. The RNG $k-\epsilon$ model still predicts the profile shape required at locations a and b, whereas the remaining turbulence models exhibit a shape closer to the positive velocity gradient found at locations d-g in the experiments. This could suggest that the profile gradient changes sign too late for the RNG $k-\epsilon$ model and too early for the $k-\omega$ and $k-\omega$ SST models.

At location d, all of the turbulence models follow a similar shape to the experimental data although the $k-\omega$ and $k-\omega$ SST models both over-predict the magnitude of the undertow. The RMSE values show that the nonlinear $k-\epsilon$ and RSM models perform the best, with the no turbulence model case performing very poorly. This pattern generally continues throughout the remaining sampling locations (e-g) except that like the $k-\omega$ models, the RNG $k-\epsilon$ model also over-estimates the velocity profile near the bottom significantly.

Although the RNG $k-\epsilon$ model performs best near the breaking point, the nonlinear $k-\epsilon$ gives the best results overall, implying that it could be important to assume anisotropic turbulence, which is further backed up by the RSM being the second best model for mean horizontal velocity profiles.

Figure 6 shows the time averaged TKE, $\overline{k}$ ($\mathrm{m^2\,s^{-2}}$), profiles with dimensionless depth for the spilling breakers case. Once again, the dots represent the experimental data collected by Ting and Kirby (1994) and the lines indicate the predictions by each of the turbulence models. Each subplot represents a different sampling location relative to the breaking point. Locations a and b are near the breaking point (5.945 and 6.665 m in Ting and Kirby (1994)), whereas the remaining sampling points are placed after breaking has occurred and correspond to locations 7.275, 7.885, 8.495, 9.11 and 9.725 m in Ting and Kirby (1994). However, Ting and Kirby (1994) only provided TKE results for the post-breaking locations, presumably because there was no turbulence prior to breaking. As can be seen in plots a and b, the RNG $k-\epsilon$ model predicts very little TKE across the whole water column, whereas every other model predicts

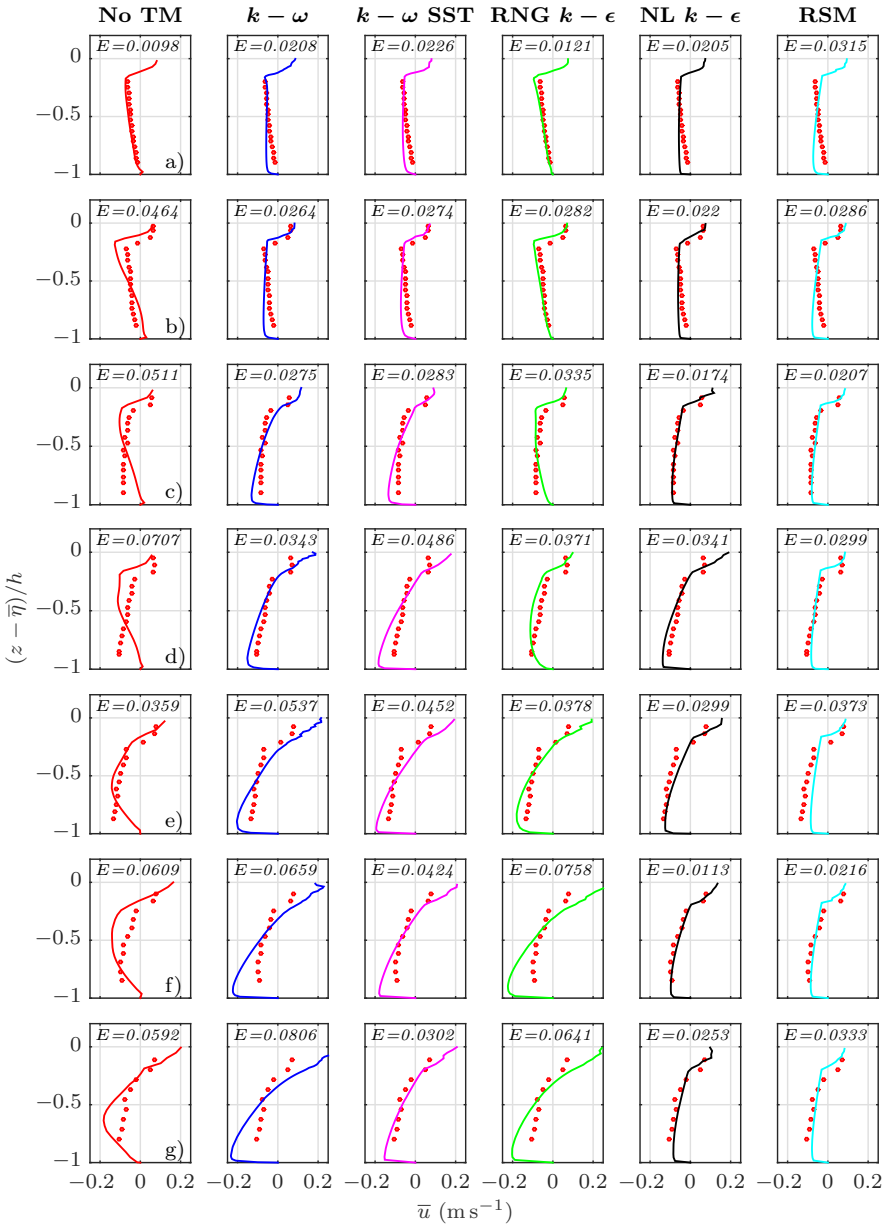

Figure 5: Comparison of time averaged velocity profiles with depth for the spilling breakers against the experimental data (dots) reported by Ting and Kirby (1994). The RMSE for each profile with respect to the experiments is indicated at the top of each plot (denoted by E). Each column represents a different turbulence model whereas the rows represent different sampling locations relative to the breaking point $x - x_b$ = a) -0.455, b) 0.265, c) 0.875, d) 1.485, e) 2.095, f) 2.71 and g) 3.325 m.

$x - x_b$ (m)	$k - \omega$	$k - \omega$ SST	RNG $k - \epsilon$	NL $k - \epsilon$	RSM
0.875	0.0035	0.0021	0.0021	0.0036	0.0096
1.485	0.0025	0.0045	0.0048	0.0047	0.0076
2.095	0.0005	0.0080	0.0009	0.0061	0.0117
2.71	0.0013	0.0060	0.0064	0.0018	0.0129
3.325	0.0026	0.0046	0.0119	0.0003	0.0099

Table 3: Root mean squared error associated with the TKE predictions for spilling breakers, with respect to the experimental data gathered by Ting and Kirby (1994). All of the different turbulence model predictions at the five locations where data is available are presented and correspond to plots c-g in Figure 6.

levels similar to after breaking has occurred. Since this occurs at the locations where the RNG $k - \epsilon$ model was the only one to capture the velocity profile, this could imply that there is a correlation between models which predict very small levels of TKE prior to breaking, and the negative gradient in the velocity profile exhibited by the unbroken wave. Furthermore, the experimental profile at location a was captured when no turbulence was assumed, which backs up the hypothesis that a turbulence model must be able to predict low levels of TKE prior to breaking.

For the five remaining sampling locations, where experimental data is available, the RMSE has been calculated for each turbulence model and is recorded in Table 3. Together with Figure 6, it is clear that all of the models generally over-estimate the levels of TKE. However, the $k - \omega$ model performs well and is the most accurate of the models overall. The $k - \omega$ SST model obtains good accuracy at the sampling locations closer to the breaking point (subplots c and d) but progressively over-estimates the magnitude further down the flume. The RNG $k - \epsilon$ model follows a similar pattern, it begins by under-estimating the TKE in subplots c and d and then over-estimates in subplots f and g. Finally, the nonlinear $k - \epsilon$ model gives similar results to the $k - \omega$ model, except at locations d and e where it significantly over-predicts the magnitude of the TKE. Interestingly, the RSM, which was expected to be the most accurate significantly over-estimates the TKE everywhere that has been sampled, leading to much larger RMSE values than the other models, despite giving reasonable results for both surface elevation and undertow.

In summary, for the spilling breakers, the different models which have been evaluated vary in performance over the three criteria considered. The RSM performed well on both surface elevation and velocity but significantly over-estimates levels of TKE. On the other hand, the $k - \omega$ model performs well for TKE and surface elevation but over-estimates the magnitude of the undertow. Overall, the most consistent model is the nonlinear $k - \epsilon$, which performs reasonably well for all three criteria.

4.2. Plunging Breakers

Tests are now performed for the plunging breakers case. Comparisons between the model predictions and observations by Ting and Kirby (1994), under

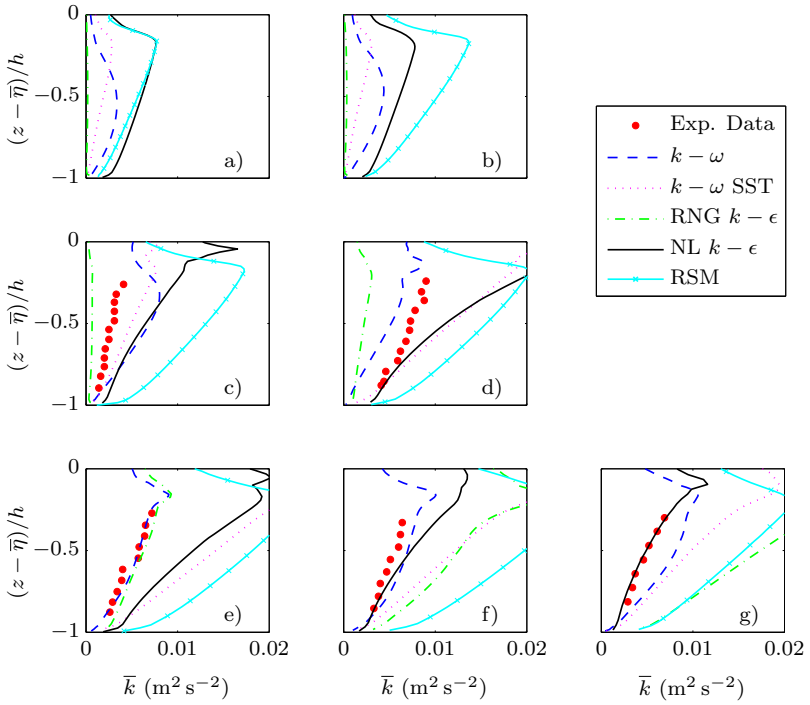

Figure 6: Comparison of time averaged TKE profiles with depth for the spilling breakers at sampling locations relative to the breaking point $x - x_b$ = a) -0.455, b) 0.265, c) 0.875, d) 1.485, e) 2.095, f) 2.71 and g) 3.325 m. Each line represents a different turbulence closure model and the dots represent the experimental data gathered by Ting and Kirby (1994).

the same wave conditions, for the maximum, mean and minimum surface elevation (Figure 7), for the time averaged velocity (Figure 8), and for mean turbulent kinetic energy profiles (Figure 9), are presented.

Figure 7 shows the same surface elevation profiles presented in Figure 2, except for the plunging breaker results. Again, each subplot compares a different turbulence closure model, a) No turbulence model, b) $k-\omega$, c) $k-\omega$ SST, d) RNG $k-\epsilon$, e) nonlinear $k-\epsilon$ and f) RSM, to the experimental data (dots) gathered by Ting and Kirby (1994) with the overall RMSE (for minimum, mean and maximum profiles combined) indicated by E in each plot. The results for the minimum and mean surface elevation profiles follow a similar pattern to the spilling breakers case. There is not much to choose between the different turbulence models since they all predict the minimum surface elevation accurately, although, there is significantly more variation in the no turbulence model and RNG $k-\epsilon$ model cases, suggesting that the waves are less repeatable, which was also observed in the spilling breakers. The $\overline{\eta}$ profile implies that the wave setup occurs at a similar rate as shown in the experimental data and is therefore

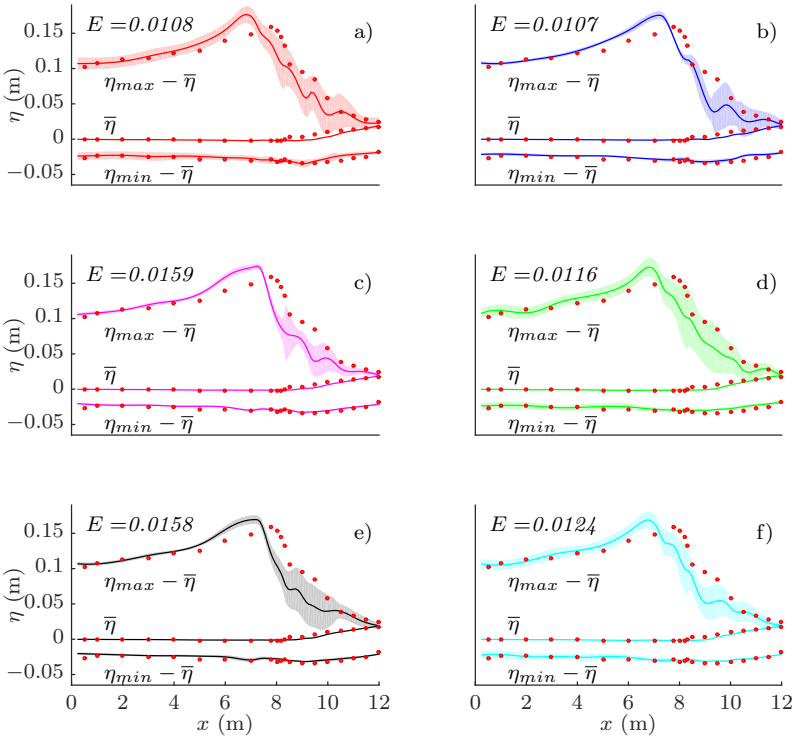

Figure 7: Comparison of surface elevation profiles $\overline{\eta}$, $\eta_{max} - \overline{\eta}$ and $\eta_{min} - \overline{\eta}$ for the plunging breakers. Each subplot represents a different model: a) No Turbulence Model, b) $k - \omega$, c) $k - \omega$ SST, d) RNG $k - \epsilon$, e) NL $k - \epsilon$, f) RSM, with an overall RMSE value, E (representing the maximum, minimum and mean profiles combined), given with respect to the laboratory data collected by Ting and Kirby (1994), indicated by the dots. One standard deviation either side of the maximum and minimum surface elevations is indicated by the shaded area.

slightly more accurate than was seen in the spilling breakers. It seems that once again, the wave setup is more accurately captured when a turbulence model is used since it occurs further down the wave flume than shown in the laboratory data when a dummy turbulence model is used.

When the maximum surface elevation profile is considered it is clear that there is much less variation between the different models than was seen in the spilling breakers (see Figure 2). This is reflected in the RMSE values, which are all very similar. All of the models shown, including the zero turbulence case, predict the waves to break a little earlier in the wave flume than was shown in the experimental data, as well as over-estimating the breaking height. Once again the RNG $k - \epsilon$ model seems to follow the profile shape and variation when no turbulence model is used, especially prior to breaking. Although there

	No TM	$k-\omega$	$k-\omega$ SST	RNG $k-\epsilon$	NL $k-\epsilon$	RSM	Ting (1994)
x_b	6.85	7.25	7.25	6.85	7.15	6.75	7.795
d_b	0.1843	0.1729	0.1729	0.1843	0.1757	0.1871	0.1573
ξ_b	-0.0018	-0.0013	-0.0013	-0.0016	-0.0011	-0.0015	-0.0022
h_b	0.1825	0.1715	0.1716	0.1827	0.1746	0.1856	0.1550
H_b	0.2040	0.2042	0.2031	0.2007	0.1976	0.1973	0.1887

Table 4: Summary of the plunging breakers information at the breaking point for each turbulence model. x_b is the breaking point, d_b, h_b are the depth from the SWL ($z = 0\,\mathrm{m}$) and MWL ($z = \xi_b\,\mathrm{m}$), respectively, and H_b is the wave height at breaking.

is not much to choose between the models in terms of profile shape, there are large differences in the variation of the maximum and minimum profiles, which follows the observations made in the spilling breakers. All of the models have smaller variation before breaking, with a much larger variation in wave shape occurring further down the tank (between 8 and 10 m). As previously discussed (see Figures 3 and 4 for the time series for spilling breakers) this pattern implies that the waves are much more repeatable before breaking than after, as is to be expected. Out of all the models, the RNG $k-\epsilon$ model appears to have a slightly larger standard deviation prior to breaking, suggesting a variation in wave shape even when the wave has not broken. The nonlinear $k-\epsilon$, $k-\omega$ and $k-\omega$ SST models have very small variation as the wave starts going up the slope, suggesting the waves are almost identical as would generally be expected. Interestingly, the upper envelope follows the turbulent bore region from the experiments for many of the turbulence models, especially the RNG $k-\epsilon$.

In summary there does not appear to be a model which captures the free surface of plunging breakers significantly better than the others, although the variation before breaking suggests that the waves are much more repeatable in the $k-\omega$, $k-\omega$ SST and nonlinear $k-\epsilon$ models.

Figure 8 shows the same mean horizontal velocity, $\overline{u}$, presented in Figure 5, except for the results of the plunging breakers. Each row of subplots indicates a different sampling location relative to the breaking point; location a is prior to the breaking point (7.295 m in Ting and Kirby (1994)), location b is at the breaking point (7.795 m in Ting and Kirby (1994))and locations c-g are post-breaking (8.345, 8.795, 9.295, 9.795 and 10.395 m in Ting and Kirby (1994)). Similar to the spilling breaker experimental results, the mean horizontal velocity is negative over the majority of water column at all sampling locations, with a relatively small region of positive mean velocity near the free surface. Again, all of the turbulence models capture this characteristic, with particularly good results at locations a-c.

The laboratory data implies that the gradient of the horizontal velocity profile with depth is negative at locations a-c, similar to the profile seen in the spilling breakers case. This negative gradient is not captured particularly well by any of the turbulence models at location a, since all of the models over-estimate the magnitude of the velocity. All of the turbulence models have a very similar

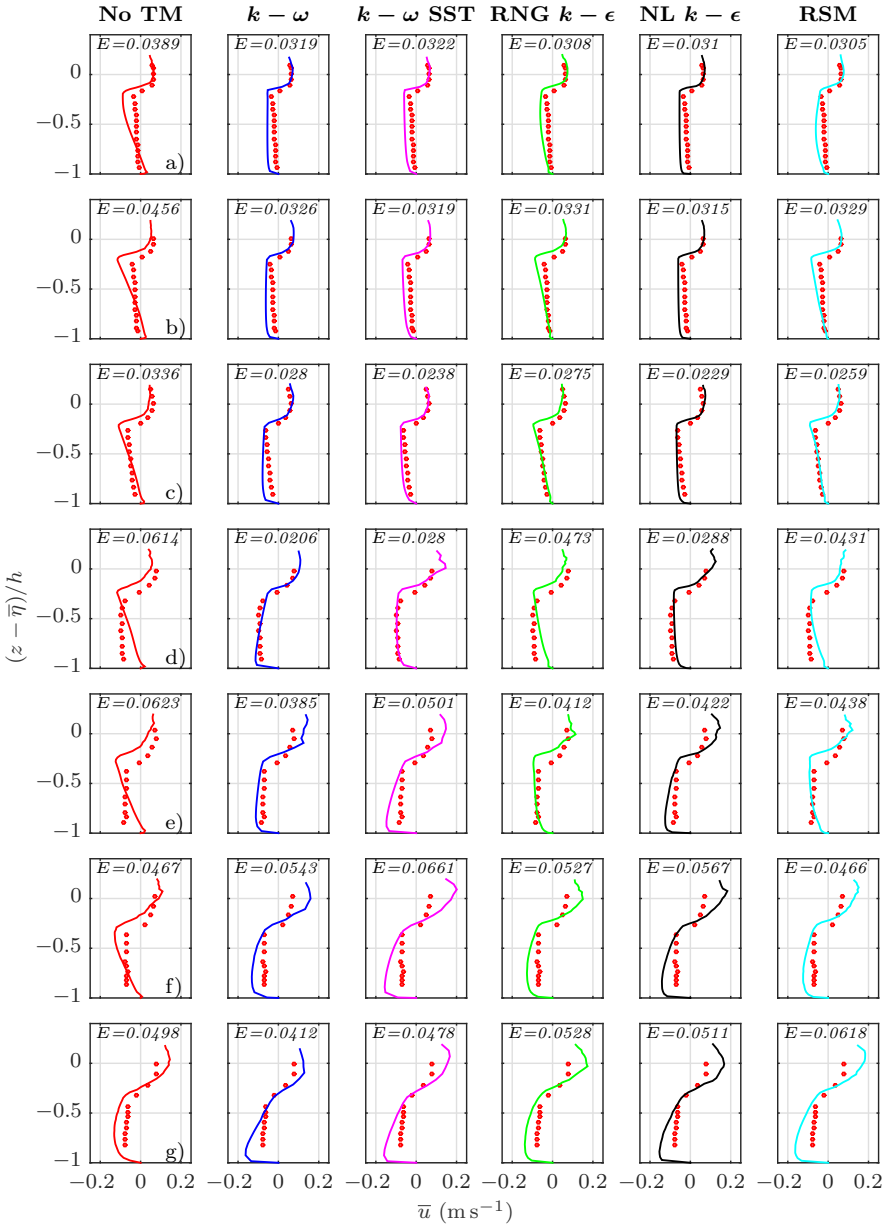

Figure 8: Comparison of time averaged velocity profiles with depth for the plunging breakers against the experimental data (dots) gathered by Ting and Kirby (1994). The RMSE for each profile with respect to the experiments is indicated at the top of each plot (denoted by E). Each column represents a different turbulence model whereas the rows represent different sampling locations relative to the breaking point $x - x_b$ = a) -0.5, b) 0.0, c) 0.55, d) 1.0, e) 1.5, f) 2.0 and g) 2.6 m.

RMSE value, but the no turbulence case performs slightly worse. However, at sampling locations b-c, the RSM and RNG $k-\epsilon$ predict a negative gradient shape, but the nonlinear $k-\epsilon$ and $k-\omega$ SST models possess the smallest RMSE. This is mainly due to the increased accuracy where the velocity changes sign near the free surface.

Contrary to the spilling breaker case, where the gradient changed sign further along the wave flume, the experimental data shows the magnitude of the mean velocity to become close to constant with depth (except near the free surface) in the plunging breaker. This is captured well at location d by the $k-\omega$, $k-\omega$ SST and nonlinear $k-\epsilon$ models. However, at locations e-f, all of these models predict a profile shape similar to that seen in the spilling breakers, i.e. the undertow is largest near the bottom of the water column and decreases with height. The RSM and RNG $k-\epsilon$ predict a similar profile shape at location d as they did for a-c and then develop much the same as the other models for the final three locations.

Overall, using the RMSE, the most accurate model for mean horizontal velocity under plunging breakers is the $k-\omega$ model, followed closely by the nonlinear $k-\epsilon$ model. The least accurate results occur when no turbulence is assumed. However, the current numerical model, in general, appears to predict the velocity profiles under spilling breakers to a greater accuracy than under plunging breakers.

Figure 9 shows the same time averaged TKE, $\overline{k}$, presented in Figure 6, except for the plunging breaker data. The subplots a-g represent the same seven locations presented in Figure 8. Furthermore, Table 5 gives the RMSE values for each of the five turbulence models, at the locations where experimental data is available. The laboratory data implies that the mean TKE has a much smaller change in depth in comparison to the spilling breakers (Figure 6), and is almost constant with depth at some of the sampling locations. None of the models capture this shape since they generally predict a significant decrease in the TKE with depth.

The RNG $k-\epsilon$ model and RSM predict very low levels of TKE at sampling locations a, b, c and d, which corresponds to the negative gradient of mean horizontal velocity with depth, observed in Figure 8. The other models have larger levels of TKE at these locations and do not capture the velocity profile. This further backs up the hypothesis from the spilling breakers that a model must predict low levels of turbulence in order to capture this profile shape.

Interestingly, the magnitude of the TKE is generally lower than observed in the spilling breakers case, and appears to increase along the wave flume at a similar rate to that shown in the experiments. The $k-\omega$ SST model performs well at location c but grows progressively larger down the flume as was seen in the spilling breakers. The nonlinear $k-\epsilon$ also follows this pattern but generally under-estimates the levels of TKE. However, it is the most consistent of the models at the sampling locations used. The remaining models generally under-predict the TKE which is reversed from the pattern seen in spilling breakers.

Overall, the nonlinear $k-\epsilon$ model predicts the TKE for plunging breakers the most accurately, followed by the $k-\omega$ model. On the other hand the

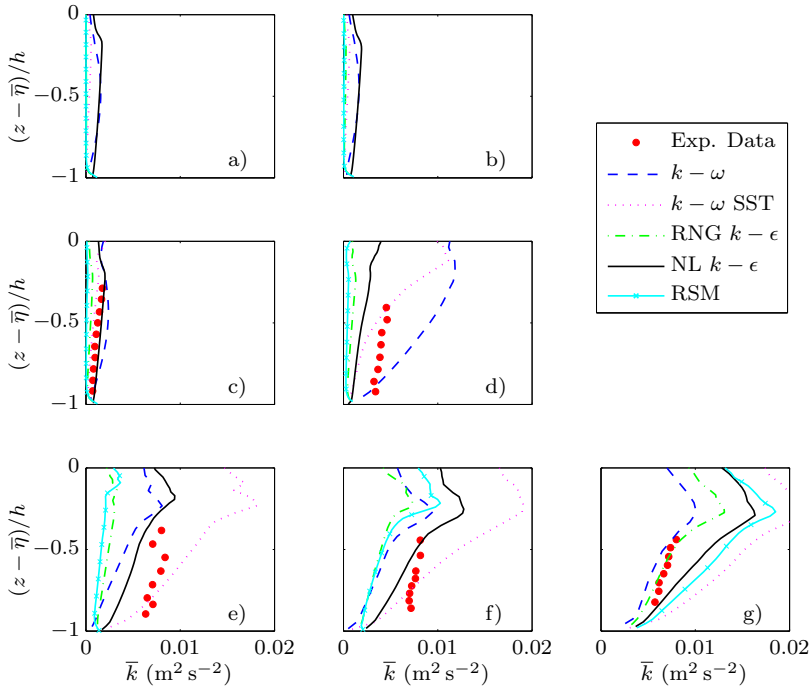

Figure 9: Comparison of time averaged TKE profiles with depth for the plunging breakers at sampling locations relative to the breaking point $x - x_b$ = a) -0.5, b) 0.0, c) 0.55, d) 1.0, e) 1.5, f) 2.0 and g) 2.6 m. Each line represents a different turbulence closure model and the dots represent the experimental data gathered by Ting and Kirby (1994).

RSM gives the least accurate results, which was also observed for the spilling breakers. However, the lack of accuracy is due to an under-estimate for the plunging breaker whereas in the spilling breaker there was a significant over-estimate.

4.3. Discussion

Choosing a numerical model is usually a balance of accuracy and numerical efficiency. In this section, both of these aspects are evaluated relative to assuming that there is no turbulence in the surf zone. Table 6 gives the execution times along with the number of iterations relative to when no turbulence is assumed. The results were obtained by running one wave period for each turbulence model on the same computer without any other applications running. The results imply that for both the plunging and spilling breakers the execution time is reduced, compared to assuming no turbulence, by using a turbulence model. This may seem counter intuitive since each iteration should take slightly longer to compute. However, as can be seen in the table, the use

$x - x_b$ (m)	$k-\omega$	$k-\omega$ SST	RNG $k-\epsilon$	NL $k-\epsilon$	RSM
0.55	0.0008	0.0005	0.0008	0.0003	0.0011
1.00	0.0034	0.0018	0.0032	0.0024	0.0036
1.50	0.0044	0.0026	0.0054	0.0028	0.0060
2.00	0.0041	0.0025	0.0044	0.0018	0.0043
2.60	0.0012	0.0064	0.0005	0.0030	0.0044

Table 5: Root mean squared error associated with the TKE predictions for plunging breakers, with respect to the experimental data gathered by Ting and Kirby (1994). All of the different turbulence model predictions at the five locations where data is available are presented and correspond to plots c-g in Figure 9.

		$k-\omega$	$k-\omega$ SST	RNG $k-\epsilon$	NL $k-\epsilon$	RSM
Spilling	CPU Time	0.978	0.802	0.828	0.673	0.641
	Iterations	0.835	0.733	0.732	0.568	0.483
	Time/Iter.	1.171	1.095	1.132	1.184	1.328
Plunging	CPU Time	0.941	0.707	0.865	0.748	0.861
	Iterations	0.794	0.646	0.743	0.633	0.667
	Time/Iter.	1.184	1.094	1.165	1.181	1.291

Table 6: Execution time, number of iterations and time per iteration for one wave period relative to the no turbulence model case.

of a turbulence model can significantly reduce the number of iterations, which can be over half as many in some cases. For the spilling breakers, the number of iterations seems to be lower in the more complex models such as the nonlinear $k-\epsilon$ and RSM. On the other hand, in the plunging breakers there is less variation in the number of iterations. However, the time per iteration for both types of breaker are consistent and generally follow the pattern expected; the RSM, which resolves all six components of the Reynolds Stress, takes longer to compute than the models which use the isotropic assumption. Overall, based on the two breaker types considered in this work, it appears that the nonlinear $k-\epsilon$ model is the most economical since it generally requires less iterations and the time per iteration is similar to the isotropic turbulence models.

To evaluate which of the turbulence closure models is the most accurate for surf zone dynamics, a skill score (SS) is applied. The SS determines whether a model is an improvement on a reference model by using the mean square error (MSE), defined as

$$\mathrm{MSE} = \frac{1}{N}\sum_{i=1}^{N}(x_i - y_i)^2, \tag{29}$$

where y_i is the experimental data and x_i is the results from the model. Following Murphy (1988), the skill score is then defined as

$$SS = 1 - \frac{\mathrm{MSE}_{\mathrm{model}}}{\mathrm{MSE}_{\mathrm{ref}}}. \tag{30}$$

		$k-\omega$	$k-\omega$ SST	RNG $k-\epsilon$	NL $k-\epsilon$	RSM
Spilling	η	0.2232	0.0684	0.4207	0.4147	0.3156
	$\overline{u}$	0.2110	0.4919	0.2897	0.7693	0.6569
	$\overline{k}$	0.7812	-0.0620	-0.2778	0.3669	-3.0165
Plunging	η	0.0127	-1.1789	-0.1630	-1.1572	-0.3372
	$\overline{u}$	0.4434	0.2770	0.2919	0.3713	0.2902
	$\overline{k}$	0.7143	0.6662	0.6587	0.8521	0.4936
Overall		0.3229	0.3609	0.2850	0.5474	0.4541

Table 7: Turbulence model skill score for surface elevation (η), time averaged velocity ($\overline{u}$) and TKE ($\overline{k}$). The skill score is calculated using the mean square error and the no turbulence model case is used as a reference.

Hence if the model has perfect prediction it will have $SS = 1$. If the SS is positive, the model is an improvement on the reference, $SS = 0$ gives results identical to the reference and a negative SS is a decrease in accuracy from the reference. In this work the reference is chosen as the case where no turbulence is assumed. Essentially the question that is being asked is whether it is beneficial to use a turbulence model, or whether assuming no turbulence actually yields more accurate results.

Table 7 gives the SS for surface elevation (η), time averaged velocity ($\overline{u}$) and TKE ($\overline{k}$). Each turbulence model is shown for both plunging and spilling breakers and is given an overall SS. Comparing the skill scores for spilling breakers it is clear that the use of any of the turbulence models considered in this study improves the accuracy of predictions of surface elevation and time averaged horizontal velocity. However, it is interesting to note that the predictions of TKE in some cases are high enough that it is more accurate to assume there is no turbulence rather than use a turbulence model. In particular the RSM, expected to perform the best, gives very poor performance for TKE despite having reasonable predictions for free surface and velocity. The nonlinear $k-\epsilon$ and $k-\omega$ models have positive skill score for all three criterion, implying that they are better than a dummy turbulence model in all areas. The RNG and nonlinear $k-\epsilon$ models give the best performance for free surface and undertow, respectively, whereas the $k-\omega$ predicts TKE most accurately.

The skill scores for the plunging breakers tell a slightly different story. The $k-\omega$ model is the only one to perform better than the dummy turbulence model in all three criteria, although it is only a slight improvement with regards to η. All of the other models have a negative skill score for free surface and is large in the case of the $k-\omega$ SST and nonlinear $k-\epsilon$ models implying they give significantly worse results compared to assuming there is no turbulence. However, the use of a turbulence model improves all results for velocity and TKE with the $k-\omega$ and nonlinear $k-\epsilon$ being the best models in these areas, respectively.

Overall, all of the turbulence models are an improvement over assuming zero turbulence in the surf zone both in terms of accuracy and numerical efficiency.

The RSM, which was initially expected to perform the best, had the second best skill score, influenced largely by the poor prediction of TKE under spilling breakers. Despite the $k-\omega$ performing better than the reference values in all three areas for both types of breaker, the nonlinear $k-\epsilon$ model comes out as the model with the highest skill score. It was also one of the more efficient models and hence it is logical to consider it to be the best turbulence closure model for application to surf zone dynamics out of the ones considered in this study. However, all the models still exhibit differences from the experimental data, in particular the under-estimate of TKE for plunging breakers and over-estimate for spilling breakers.

These differences raise the question of the benefit of using a complex model over a computationally cheaper option such as a depth-integrated model. Although it is possible to simulate breaking waves using a depth-integrated model through the use of dissipation terms, the breaking process cannot be fully reproduced since the model is unable to resolve the overturning of the free surface (Roeber and Cheung, 2012). A RANS solver, coupled with the VOF method, is able to resolve this highly-nonlinear process. As will be seen later in this Section, capturing this process leads to predictions of turbulence generation which agree qualitatively with laboratory observations. Further advantages of the CFD approach is that data can be gathered anywhere in the domain and the model can easily be adapted for more complex phenomena such as the interaction with structures.

To understand the variation in the predictions of the turbulence models considered in this study, instantaneous spatial maps are compared qualitatively to experimental investigations. Ting and Kirby (1994) found that TKE is transported seaward under the spilling breakers and the dissipation rate is slow, whereas under the plunging breaker TKE is transported landward and is dissipated within one wave cycle. Additionally, the TKE varies with depth in the spilling case, which is not evident under the plunging waves. Furthermore, Ting and Kirby (1995) found that under the crest of plunging breakers the turbulence intensity is largest and rapidly decreases after the wave passes so that the turbulence dies out between breakers. For plunging waves the rate of vertical mixing is large since turbulence is spread down by the large eddies, causing any turbulence created by the broken wave to saturate the entire depth in the inner surf zone. Ting and Kirby (1996) show that the mixing length of the spilling case is much smaller, suggesting that it lies somewhere in the region of 10-20% of the water depth. Particle Image Velocimetry data (PIV) presented by Huang et al. (2009) generally agrees with the observations of Ting and Kirby (1996) but indicates that TKE spreads to around half the water depth. Furthermore, the surface generated turbulence in spilling waves is spread slowly down, mainly through diffusion, whereas in the plunging case both advective and diffusive transport are important since the large eddies generated in the surface roller are advected behind the wave front.

Many of these observed characteristics are also evident in the present numerical model. In a RANS simulation, small scale features are not resolved but fluctuations from the mean flow are instead represented by an additional dissi-

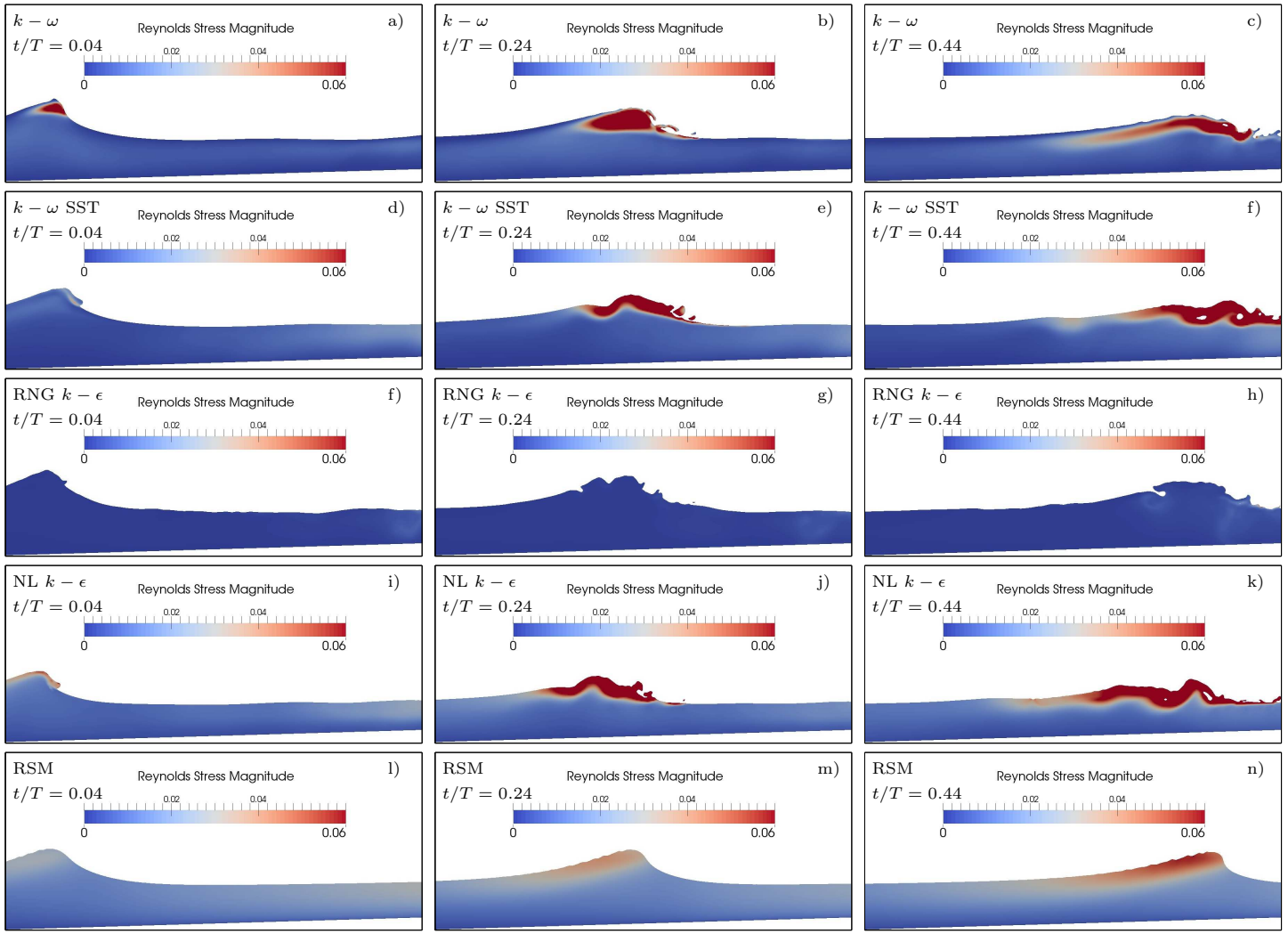

Figure 10: Example snapshots of the Reynolds stress (magnitude) distribution under spilling breakers with each row representing a different turbulence model. From left to right the columns show different phases of the wave: $t/T = 0.04$, 0.24 and 0.44, respectively.

pation term in the governing equations. This term is generally referred to as the Reynolds stress (see equation 6) and is related to the TKE, eddy viscosity and rate of strain of the flow. Therefore, for the current work, the Reynolds stress is a good indication of the presence of turbulence in the flow. Furthermore, it was found that the distributions of TKE and Reynolds stress (magnitude) followed very similar patterns for all of the turbulence models considered. Therefore, this allows qualitative comparison of the predicted (numerical) Reynolds stress with either TKE or Reynolds stress from experiments.

Figure 10 shows colour plots of the predicted Reynolds stress magnitude for spilling breakers using the different turbulence models (rows) at three different phases of the breaking process (columns). The phase $t/T = 0$ is considered to be the phase where breaking occurs. It is clear that both the magnitude and distribution of the Reynolds stress varies between the different turbulence models. The RNG $k-\epsilon$ model predicts smaller Reynolds stress magnitude than the other four models at all of the three times presented. However, there is a region near the right hand side of each plot where there is a relatively larger Reynolds stress, indicating that the turbulence from the previous wave has not dissipated. The other four models generate turbulence in the crest during the breaking process and as the wave passes the turbulence spreads slowly seaward and downwards, which is consistent with the observations of Ting and Kirby (1996) and the PIV experiments conducted by Huang et al. (2009). At the first breaking phase shown, the $k-\omega$ model predicts a large region of high Reynolds stress spanning the majority of the front of the wave crest. The $k-\omega$ SST and nonlinear $k-\epsilon$ models predict the Reynolds stress to be generated in the spilling region of the wave. The predictions from the $k-\omega$ and $k-\omega$ SST models in the other two phases of the wave ($t/T = 0.24$ and 0.44) indicate that the turbulence spreads to around 20% of the water depth, which is consistent with Ting and Kirby (1996) but conflicts with Huang et al. (2009). Conversely, the RSM and nonlinear $k-\epsilon$ predictions of Reynolds stress indicate that there is always a reasonable level throughout the water column. Furthermore, the distribution of the Reynolds stress predicted by the RSM, i.e. large turbulence throughout the wave, seems to lead to the wave not visibly breaking.

Figure 11 presents τ_{xz}, i.e. the horizontal-vertical component of Reynolds stress, under spilling breakers at $t/T = 0.44$. Each plot represents a different turbulence model; a) $k-\omega$, b) $k-\omega$ SST, c) RNG $k-\epsilon$, d) nonlinear $k-\epsilon$ and e) RSM. The $k-\omega$, $k-\omega$ SST and nonlinear $k-\epsilon$ predict similar distributions of τ_{xz}, and generally agree with experimental studies of weak hydraulic jumps, which are believed to be a simplified method to study the flow under spilling breakers in the inner surf zone (Misra et al., 2008). Like the experimental data for hydraulic jumps, there are two clear regions in the spilling breaker; the reverse flow region and the breaker shear layer region. In the reverse flow region τ_{xz} is much smaller than in the breaker shear layer, which is consistent with Misra et al. (2008). In the breaker shear layer, τ_{xz} is predominantly negative, with the largest magnitude occurring just below the free surface near the toe of the breaker, which agrees with experimental data (see Figures 18d and 19 of Misra et al. (2008)). Further similarities can be observed at the free surface

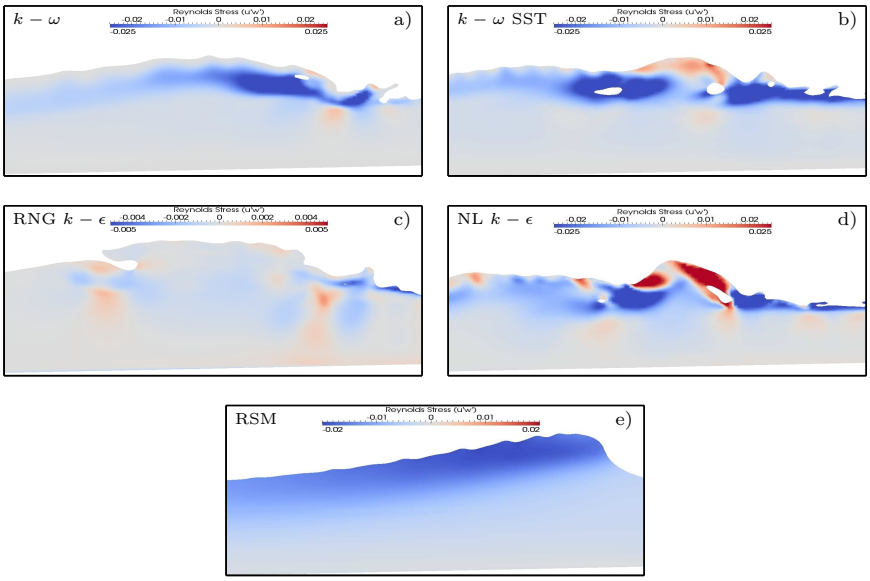

Figure 11: Snapshots of τ_{xz} under spilling breakers at $t/T = 0.44$. Each plot is a different turbulence model; a) $k-\omega$, b) $k-\omega$ SST, c) RNG $k-\epsilon$, d) nonlinear $k-\epsilon$ and e) RSM.

where a layer of positive τ_{xz} is present. At the toe, the breaker shear layer is relatively thin but behind the front the region of Reynolds stress spreads out to incorporate more of the water depth and decreases in magnitude. The width of the breaker shear layer was observed to be around 20% of the water depth by Misra et al. (2008), which is consistent with the predictions presented in Figure 11. Overall, the numerical model appears to have good qualitative agreement with experimental data for a similar flow, which both validates the current model and provides evidence that weak hydraulic jumps are a valid representation of spilling breakers.

Figure 12 presents similar spatial maps of the Reynolds stress magnitude as described in Figure 10 for the plunging breakers case. At the breaking point the predictions from the nonlinear $k-\epsilon$, $k-\omega$ SST and RSM model indicate that turbulence is generated from the impact of the overturning wave hitting the water and causing splash up. Conversely, the $k-\omega$ model predicts Reynolds stress to be generated throughout the crest of the wave as was observed in the spilling breaker. Another similarity to the spilling case is that the RNG $k-\epsilon$ model predicts the smallest Reynolds stress out of the turbulence models. However, the model predicts significantly larger regions of Reynolds stress, particularly in the areas where air has become trapped, and the turbulence spreads the whole depth of the water column as can be seen at the right hand side of the phase $t/T = 0.36$ (plot h). At phase $t/T = 0.2$ it is clear that any entrapped air leads to large Reynolds stress predictions by all of the models. The turbulence gener-

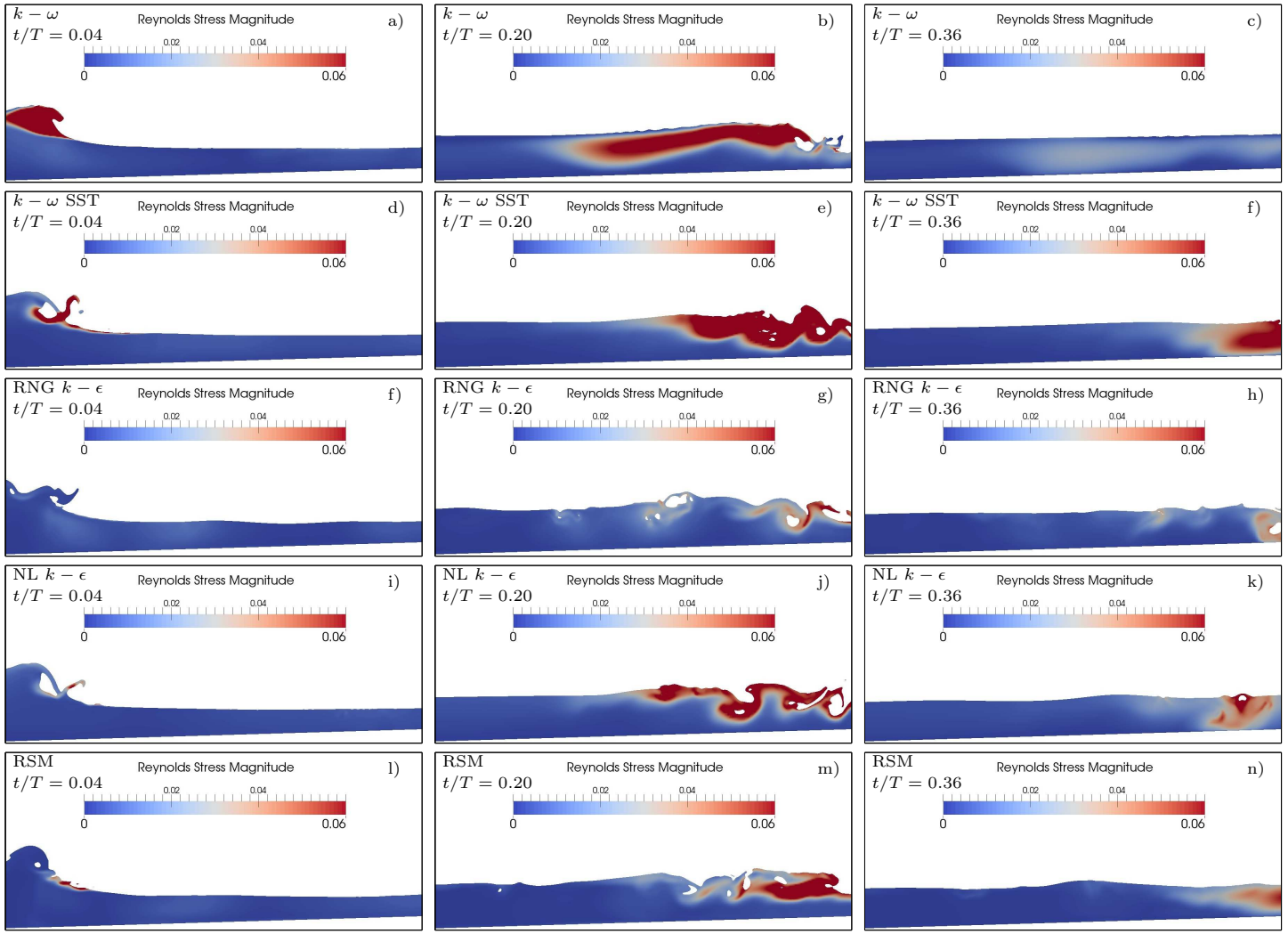

Figure 12: Example snapshots of the Reynolds stress (magnitude) distribution under plunging breakers with each row representing a different turbulence model. From left to right the columns show different phases of the wave: $t/T = 0.04$, 0.20 and 0.36, respectively.

ally remains with the wave front and can be seen to be advected with the flow. At the $t/T = 0.36$ phase, all of the models considered in this study predict the turbulence to spread over the whole water depth, which also agrees well with the description given by Ting and Kirby (1995). The PIV experiments of Kimmoun and Branger (2007), showed that the Reynolds stress saturates the water depth in the turbulent bore whilst little turbulence occurred below the trough level at the breaking point. This is consistent with all of the models considered in this study. Interestingly, the $k - \omega$ model has a region of Reynolds stress which breaks off from the wave front and remains in the water column (centre of plot c). The detached region resembles observations from PIV experiments of unsteady deep-water breaking waves (Melville et al., 2002; Drazen and Melville, 2009). The experimental results implied that the turbulence starts at the top of the water column and diffuses downwards after the wave has passed. Although only the magnitude is shown in Figure 12, the horizontal-vertical component τ_{xz}, is negative and is therefore consistent with downward transport of positive horizontal momentum and hence PIV experiments (Melville et al., 2002; Drazen and Melville, 2009). This region of turbulence occurs where there is a change between the positive velocity of the passing wave and the undertow preceding the next wave, and rapidly dissipates before the next wave occurs, similar to the observations of Ting and Kirby (1995).

Figures 13 and 14 show additional spatial maps of Reynolds stress magnitude at further phases of the breaking process for spilling and plunging breakers, respectively. The nonlinear $k-\epsilon$ model is used for this analysis since it has been shown to have the best overall skill score. At the breaking phase ($t/T = 0.00$), there is a large difference between the two breaking types. The spilling breaker has Reynolds stress already existing in the water column, whereas the plunging breaker has very little. This implies that the turbulence from the previous wave has dissipated in the plunging breaker, whereas it has not in the spilling breaker as was observed by Ting and Kirby (1994). Furthermore, there is a small amount of Reynolds stress existing in the water column under the spilling breaker prior to breaking, while it is not apparent in the plunging case. This could be due to turbulence being transported seaward as was noted in Ting and Kirby (1994).

Phases $t/T = 0.16$ to 0.32 show another characteristic observed by Ting and Kirby (1995, 1996). In the plunging breaker, as the surface roller develops, turbulence spreads rapidly downwards spanning the whole depth around phase $t/T = 0.24$. The turbulence rapidly dissipates after the surface roller has passed, explaining the small magnitude of Reynolds stress observed by the time the next wave arrives. On the other hand, there is a fairly large level of turbulence existing in the water column as the spilling breaker arrives. As the surface roller progresses down the wave flume, the turbulence generated in the spilling breaker slowly spreads seawards and downwards from the roller. This leads to larger concentrations near the surface, which decrease with depth. The majority of the turbulence is shown to be located in the near surface region as was observed in the experiments of Ting and Kirby (1995).

In the latter phases presented in Figures 13 and 14 ($t/T = 0.48$ to 0.56), it is clear that the turbulence rapidly dissipates once the surface roller has passed in

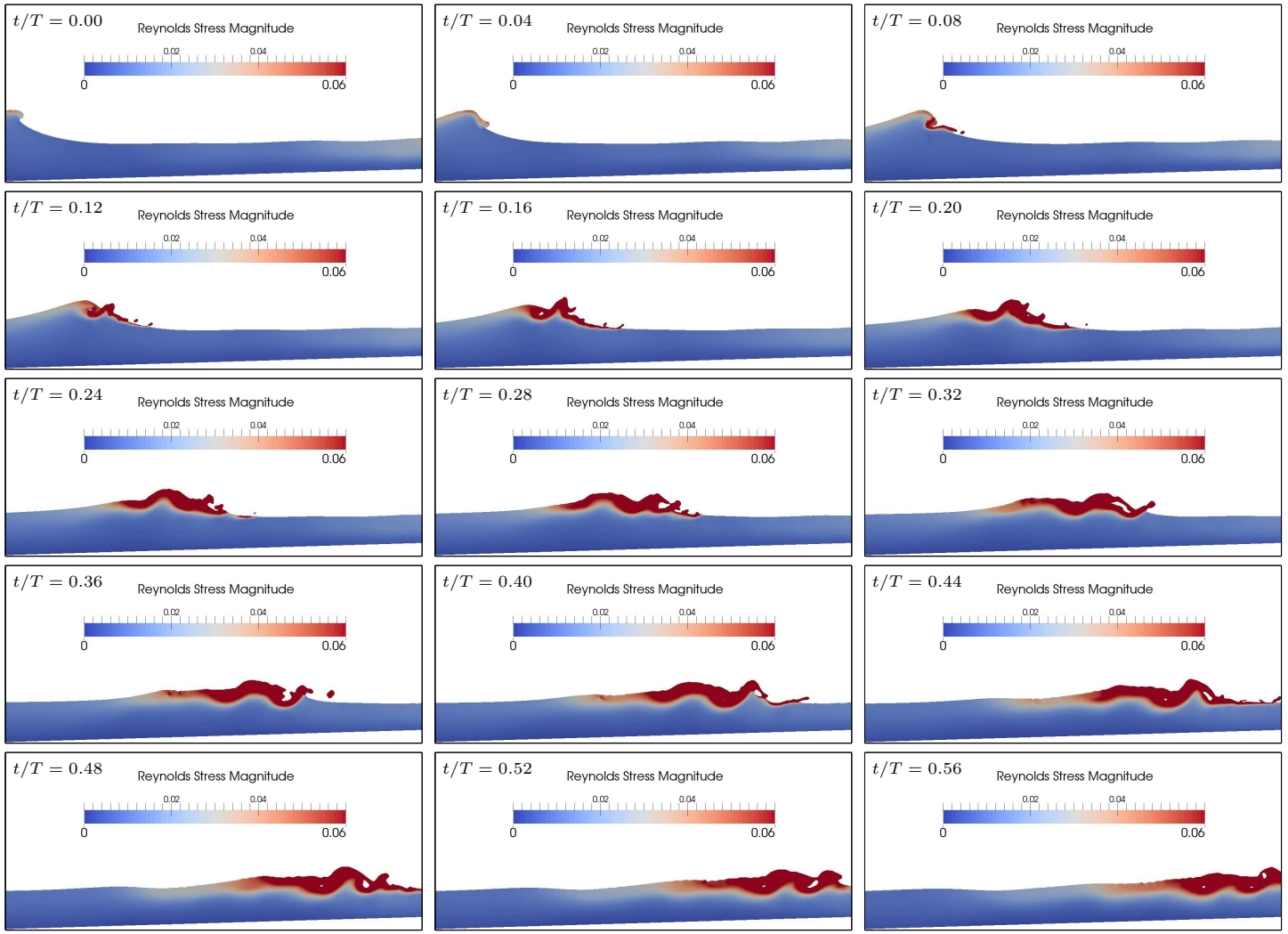

Figure 13: Snapshots of the nonlinear $k - \epsilon$'s predictions of the Reynolds stress (magnitude) distribution under the different phases ($t/T = 0$ to $t/T = 0.56$) of a spilling breaker.

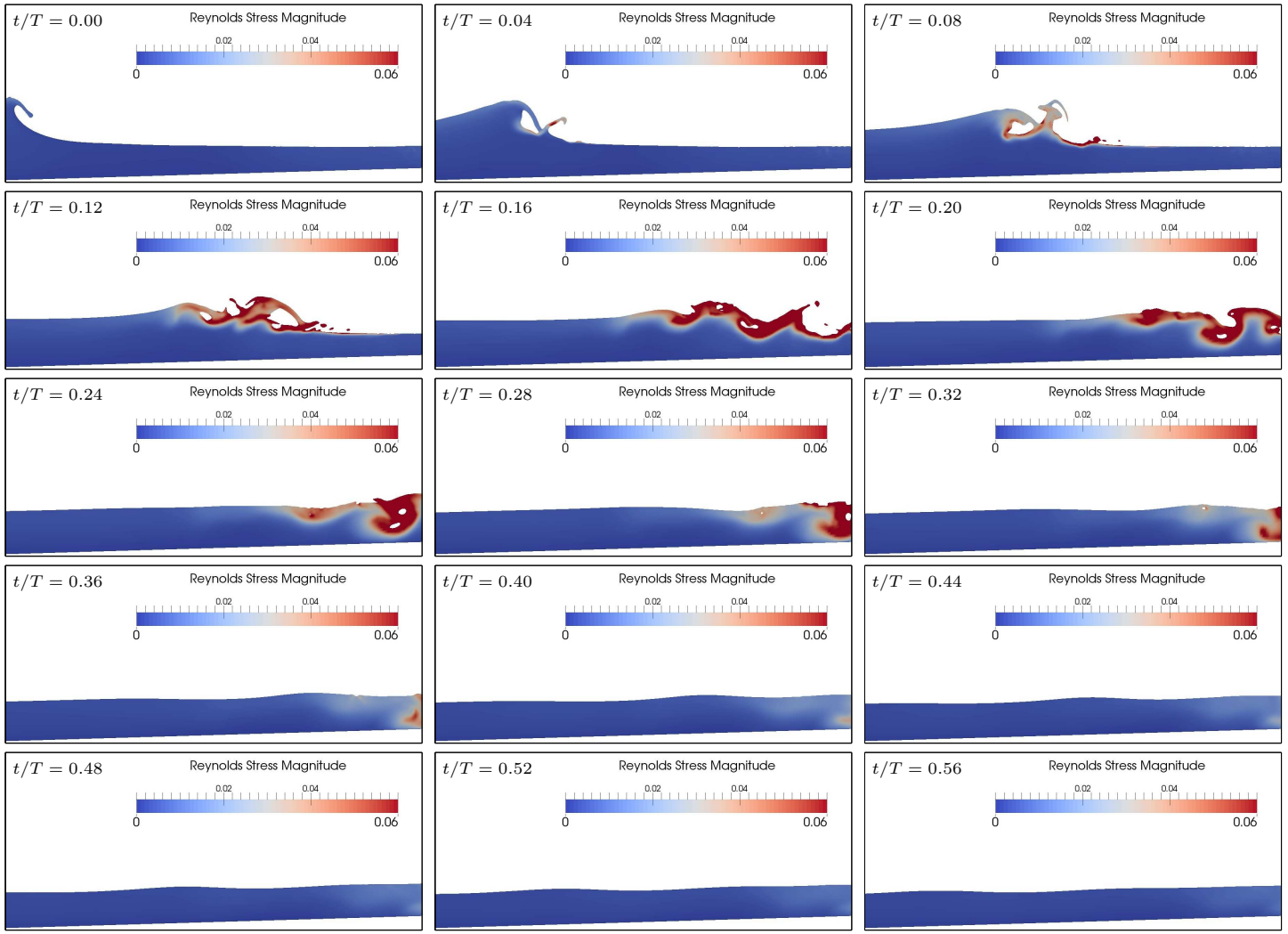

Figure 14: Snapshots of the nonlinear $k - \epsilon$'s predictions of the Reynolds stress (magnitude) distribution under the different phases ($t/T = 0$ to $t/T = 0.56$) of a plunging breaker.

the plunging breaker, whereas it spreads out behind the spilling breaker. This leads to turbulence from the previous wave interacting with the next wave. This could be due to the shorter period of the wave. Hence, in the future, it would be interesting to repeat the analysis on the two breaker types if the beach slope has been adjusted and wave period kept constant. In summary, the present numerical model generally predicts similar turbulent characteristics to those seen in laboratory experiments. The spatial maps also imply that a number of turbulence models used in this study agree qualitatively with experimental studies but require further research in order to gain better quantitative agreement.

5. Conclusion

In this work, a new library of turbulence closure models for multiphase flows has been evaluated for application to surf zone dynamics using the open source CFD software, OpenFOAM, along with the additional toolbox, waves2Foam. The models were averaged over twenty wave periods and compared to previous experimental data. The models were evaluated both in terms of accuracy (for surface elevation, velocity and TKE) and numerical efficiency using zero turbulence as a reference. It was found that using a turbulence model could significantly decrease the computational time since although each iteration took longer to compute, the simulation required less iterations.

To assess accuracy, a skill score based on the mean squared error was used in order to evaluate which of the turbulence models is the best. Interestingly, it was found that assuming no turbulence lead to more accurate predictions of TKE levels under spilling breakers than some of the turbulence models since they over-predicted these quantities significantly. However, using a turbulence model generally improved the free surface and undertow profiles in the spilling breakers. There appears to be a correlation between models which predict very little TKE prior to breaking and models which capture a negative gradient of velocity prior to breaking, as observed in the experiments. The RNG $k-\epsilon$ model is the only model to capture this profile shape in both plunging and spilling breakers. However, the nonlinear $k-\epsilon$ model captures the velocity profiles more accurately over the whole surf zone. For plunging breakers, using a turbulence model improves the TKE and velocity profiles but generally decreases the accuracy of the free surface predictions. Despite the RSM being expected to produce the best results, it gave very poor predictions of TKE in spilling breakers leading to a smaller skill score compared to the nonlinear $k-\epsilon$ model. The $k-\omega$ model was shown to be the only model to improve on the zero turbulence case in all criteria. However, in this study the overall best model for surf zone dynamics, both in terms of accuracy and numerical efficiency, was found to be the nonlinear $k-\epsilon$. Based on the skill score alone the ranking of the turbulence models would be:

1. Nonlinear $k-\epsilon$
2. RSM
3. $k-\omega$ SST

4. $k - \omega$
5. RNG $k - \epsilon$

Spatial maps of the Reynolds stress magnitude distribution were then used to compare the turbulence models predictions for both breaker types. The spilling breaker was shown to have good qualitative agreement with experimental data on weak hydraulic jumps. The nonlinear $k - \epsilon$ model was then shown to exhibit many of the features noted in the experimental data relating to the transport of turbulence under different breaker types. The turbulence spread over the whole water depth before rapidly dissipating prior to the arrival of the next plunging breaker. On the other hand, the spilling breakers turbulence spread seaward and only slowly diffused downwards. Slow dissipation in this case led to turbulence generated by a wave still existing in the water column when the following wave arrives.

In the future, it would be interesting to repeat the analysis on the two breaker types in cases where the beach slope has been adjusted and wave period kept constant. This would allow more thorough analysis as to the cause of the slow dissipation rate in the spilling breaker. Another interesting test would be to compare the results presented here to large eddy simulations, to see whether the results, in particular the TKE profiles, improve enough to justify the increase in computational effort.

Acknowledgements

The authors would like to thank the School of Marine Science and Engineering at Plymouth University for their financial support throughout this research. This work was conducted using the HPC facility at Plymouth University and the authors gratefully acknowledge Peter Mills for his continual support with this resource.

References

Battjes, J. A., 1974. Surf similarity. In: Proceedings of the 14^{th} International Conference on Coastal Engineering. pp. 466–480.

Bradford, S. F., 2000. Numerical simulation of surf zone dynamics. J. Waterw. Port. C-ASCE 126.

Brown, S. A., Magar, V., Greaves, D. M., Conley, D. C., 2014. An evaluation of rans turbulence closure models for spilling breakers. In: Proceedings of the 34^{th} International Conference on Coastal Engineering. Vol. 1. p. 5.

Christensen, E. D., Jensen, J. H., Mayer, S., 2000. Sediment transport under breaking waves. In: Proceedings of the 27^{th} International Conference on Coastal Engineering. Vol. III. pp. 2467–2480.

Drazen, D. A., Melville, W. K., 2009. Turbulence and mixing in unsteady breaking surface waves. J. Fluid Mech. 628, 85–119.

Falchetti, S., Conley, D. C., Brocchini, M., Elgar, S., 2010. Nearshore bar migration and sediment-induced buoyancy effects. Continental Shelf Research 30, 226–238.

Govender, K., Mocke, G. P., Alport, M. J., 2002. Video-imaged surf zone wave and roller structures and flow fields. J. Geophys. Res. 107 (C7), 9–1 – 9–21.

Huang, Z.-C., Hsiao, S.-C., Hwung, H.-H., Chang, K.-A., 2009. Turbulence and energy dissipations of surf-zone spilling breakers. Coastal Eng. 56, 733–746.

Iribarren, C. R., Nogales, C., 1949. Protection de ports. In: XVIIth Int. Nav. Congress,. Vol. II. pp. 31–80.

Jacobsen, N. G., 2011. A full hydro- and morphodynamic description of breaker bar development. Ph.D. thesis, Technical University of Denmark, Department of Mechanical Engineering, dCAMM Special Report, no. S136.

Jacobsen, N. G., Fuhrman, D. R., Fredsøe, J., 2012. A wave generation toolbox for the open-source CFD library: OpenFoam®. Int. J. Numer. Meth. Fluids. 70, 1073–1088.

Kimmoun, O., Branger, H., 2007. A particle image velocimetry investigation on laboratory surf-zone breaking waves over a sloping beach. J. Fluid Mech. 588, 353–397.

Launder, B. E., Reece, G. J., Rodi, W., 1975. Progress in the development of a reynolds-stress turbulence closure. J. Fluid Mech. 68 (3), 537–566.

Lin, P., Liu, P. L. F., 1998a. A numerical study of breaking waves in the surf zone. J. Fluid Mech. 359, 239–264.

Lin, P., Liu, P. L. F., 1998b. Turbulence transport, vorticity dynamics and solute mixing under plunging waves in surf zone. J. Geophys. Res. 103 (C8), 15677–15694.

Ma, G., Chou, Y., Shi, F., 2014. A wave-resolving model for nearshore suspended sediment transport. Ocean Modell. 77, 33–49.

Melville, W. K., Veron, F., White, C. J., 2002. The velocity field under breaking waves: coherent structures and turbulence. J. Fluid Mech. 454, 203–233.

Menter, F. R., 1994. Two-equation eddy-viscosity turbulence models for engineering applications. AIAA Journal 32 (8), 1598–1605.

Misra, S. K., Kirby, J. T., Brocchini, M., Veron, F., Thomas, M., Kambhamettu, C., 2008. The mean turbulent flow structure of a weak hydraulic jump. Phys. Fluids 20 (035106), 21pp.

Murphy, A. H., 1988. Skill scores based on the mean square error and their relationships to the correlation coefficient. Monthly Weather Review 116, 2417–2424.

OpenFOAM, 2014. The open source CFD toolbox. http://www.openfoam.com/.

Puleo, J. A., Holland, K. T., Plant, N. G., Slinn, D. N., Hanes, D. M., 2003. Fluid acceleration effects on suspended sediment transport in the swash zone. J. Geophys. Res. 108 (C11).

Rienecker, M. M., Fenton, J. D., 1981. A Fourier approximation method for steady water waves. J. Fluid Mech. 104, 119–137.

Roeber, V., Cheung, K. F., 2012. Boussinesq-type model for energetic breaking waves in fringing reef environments. Coastal Eng. 70, 1–20.

Shih, T. H., Zhu, J., Lumley, J. L., 1996. Calculation of wall-bounded complex flows and free shear flows. Int. J. Numer. Meth. Fl. 23, 1133–1144.

Speziale, C. G., Thangam, S., 1992. Analysis of an RNG based turbulence model for separated flows. Int. J. Eng. Sci. 30 (10), 1379–1388.

Ting, F. C. K., Kirby, J. T., 1994. Observation of undertow and turbulence in a laboratory surf zone. Coastal Eng. 24, 51–80.

Ting, F. C. K., Kirby, J. T., 1995. Dynamics of surf-zone turbulence in a strong plunging breaker. Coastal Eng. 24, 177–204.

Ting, F. C. K., Kirby, J. T., 1996. Dynamics of surf-zone turbulence in a spilling breaker. Coastal Eng. 27, 131–160.

van Rijn, L. C., 2007. Unified view of sediment transport by currents and waves. II: Suspended transport. J. Hydraul. Eng. 133 (6), 668 – 689.

Versteeg, H. K., Malalasekera, W., 1995. An Introduction to Computational Fluid Dynamics: The Finite Volume Method. Pearson Education Ltd.

Wilcox, D. C., 1988. Reassessment of the scale-determining equation for advance turbulence models. AIAA Journal 26 (11), 1299–1310.

Wilcox, D. C., 2006. Turbulence Modeling for CFD, 3rd Edition. DCW Industries, inc.

Xie, Z., 2013. Two-phase flow modelling of spilling and plunging breaking waves. Applied Mathematical Modelling 37, 3698–3713.

Yakhot, V., Thangam, S., Gatski, T. B., Orszag, S. A., Speziale, C. G., 1992. Development of turbulence models for shear flows by a double expansion technique. Phys. Fluids A 4 (7), 1510 – 1520.